

# The CARMENES search for exoplanets around M dwarfs

## Not-so-fine hyperfine-split vanadium lines in cool star spectra

Y. Shan<sup>1</sup>, A. Reiners<sup>1</sup>, D. Fabbian<sup>1,2,3</sup>, E. Marfil<sup>4</sup>, D. Montes<sup>4</sup>, H. M. Tabernero<sup>5</sup>, I. Ribas<sup>6,7</sup>, J. A. Caballero<sup>5</sup>, A. Quirrenbach<sup>8</sup>, P. J. Amado<sup>9</sup>, J. Aceituno<sup>10,9</sup>, V. J. S. Béjar<sup>11,12</sup>, M. Cortés-Contreras<sup>5</sup>, S. Dreizler<sup>1</sup>, A. P. Hatzes<sup>13</sup>, Th. Henning<sup>14</sup>, S. V. Jeffers<sup>15,1</sup>, A. Kaminski<sup>8</sup>, M. Kürster<sup>14</sup>, M. Lafarga<sup>6,7,16</sup>, J. C. Morales<sup>6,7</sup>, E. Nagel<sup>17,13</sup>, E. Pallé<sup>11</sup>, V. M. Passegger<sup>18,17</sup>, C. Rodríguez-López<sup>9</sup>, A. Schweitzer<sup>17</sup>, and M. Zechmeister<sup>1</sup>

(Affiliations can be found after the references)

Received 11 June 2021 / Accepted 6 August 2021

### ABSTRACT

**Context.** M-dwarf spectra are complex and notoriously difficult to model, posing challenges to understanding their photospheric properties and compositions in depth. Vanadium (V) is an iron-group element whose abundance supposedly closely tracks that of iron, but has origins that are not completely understood.

**Aims.** Our aim is to characterize a series of neutral vanadium atomic absorption lines in the 800–910 nm wavelength region of high signal-to-noise, high-resolution, telluric-corrected M-dwarf spectra from the CARMENES survey. Many of these lines are prominent and exhibit a distinctive broad and flat-bottom shape, which is a result of hyperfine structure (HFS). We investigate the potential and implications of these HFS split lines for abundance analysis of cool stars.

**Methods.** With standard spectral synthesis routines, as provided by the spectroscopy software *iSpec* and the latest atomic data (including HFS) available from the VALD3 database, we modeled these striking line profiles. We used them to measure V abundances of cool dwarfs.

**Results.** We determined V abundances for 135 early M dwarfs (M0.0 V to M3.5 V) in the CARMENES guaranteed time observations sample. They exhibit a [V/Fe]-[Fe/H] trend consistent with that derived from nearby FG dwarfs. The tight ( $\pm 0.1$  dex) correlation between [V/H] and [Fe/H] suggests the potential application of V as an alternative metallicity indicator in M dwarfs. We also show hints that neglecting to model HFS could partially explain the temperature correlation in V abundance measurements observed in previous studies of samples involving dwarf stars with  $T_{\text{eff}} \lesssim 5300$  K.

**Conclusions.** Our work suggests that HFS can impact certain absorption lines in cool photospheres more severely than in Sun-like ones. Therefore, we advocate that HFS should be carefully treated in abundance studies in stars cooler than  $\sim 5000$  K. On the other hand, strong HFS split lines in high-resolution spectra present an opportunity for precision chemical analyses of large samples of cool stars. The V-to-Fe trends exhibited by the local M dwarfs continue to challenge theoretical models of V production in the Galaxy.

**Key words.** atomic data – line: profiles – techniques: spectroscopic – stars: abundances – stars: low-mass

## 1. Introduction

The analysis of detailed chemical abundances in stellar photospheres can help constrain the mechanisms of cosmic nucleosynthesis, reveal the evolution of galaxies and their stellar populations, and shed light on the formation of exoplanets (e.g., Tinsley 1980; Timmes et al. 1995; Kobayashi et al. 2006; Fabbian et al. 2009; Nomoto et al. 2013; Kobayashi et al. 2020; Fischer & Valenti 2005; Meléndez et al. 2009; Adibekyan et al. 2012; Dorn et al. 2015; Adibekyan et al. 2021). Accurate measurements require access to spectra with high resolution and high signal-to-noise (S/N), as well as robust stellar atmosphere models and comprehensive atomic data (see e.g., reviews by Allende Prieto 2016; Jofré et al. 2019).

Vanadium ( $_{23}\text{V}$ ) is an odd- $Z$  iron-peak element whose origin is not completely understood. It is thought to be chiefly produced in explosive silicon and oxygen burning in supernovae (SNe) of type II (Woosley & Weaver 1995), with type Ia SNe supposedly also contributing to a lesser extent (e.g., Clayton 2003; Bravo & Martínez-Pinedo 2012). However, when the theories are propagated through nucleosynthesis and Galactic chemical evolution (GCE) models, the predicted vanadium-to-iron ratios, [V/Fe]  $\sim -0.2$  to  $-0.5$  dex, fall significantly below those observed in

representative stellar populations, where [V/Fe] remains close to solar or slightly super-solar over a large range of metallicities (e.g., Kobayashi et al. 2011, 2020; Nomoto et al. 2013; Sneden et al. 2016).

To date, most measurements of V abundance have been performed in populations of Sun-like stars (e.g., Gratton & Sneden 1991; Feltzing & Gustafsson 1998; Prochaska et al. 2000; Reddy et al. 2003; Battistini & Bensby 2015, to name a few) or giants and subgiants (e.g., Liu et al. 2012; Roederer et al. 2014; Hawkins et al. 2016; Lomaeva et al. 2019), almost exclusively with  $T_{\text{eff}} \gtrsim 4000$  K. The majority of studies use observations in the visual wavelength range: 400–700 nm. A number of neutral and ionized V lines lie in this region, from which abundances can be constrained (and, in some cases, from as few as one single line) with either equivalent width (EW) analysis or direct spectral synthesis fits (SSF). While these combinations of data and methodology seem to generate robust results for FG-type stars, several studies whose samples included K dwarfs have found a large scatter in [V/Fe] and a systematic upward trend with decreasing effective temperature ( $T_{\text{eff}}$ ) below  $\sim 5300$  K (e.g., Bodaghee et al. 2003; Gilli et al. 2006; Neves et al. 2009; Adibekyan et al. 2012; Tabernero et al. 2012; Montes et al. 2018). This correlation has often been ascribed to model-

ing deficiencies, such as effects that are not accounted from non-local thermodynamic equilibrium (NLTE).

Incidentally,  $^{51}\text{V}$ , the most abundant isotope accounting for  $> 99\%$  of naturally occurring vanadium, has a rather high nuclear spin ( $+7/2$ ) and shows pronounced hyperfine structure (HFS), which are shifts in atomic energy levels. These shifts split atomic transitions into multiple, usually closely spaced components. The manifestation of HFS in a number of absorption lines, including those of V, was already noticed in solar spectra by Abt (1952). However, due to limitations in atomic data, and perhaps also in awareness, not all stellar population studies to date have completely accounted for HFS in their spectral modeling. Interestingly, all the aforementioned studies of K dwarfs that have observed a correlation between V abundance and  $T_{\text{eff}}$  neglected to include HFS components in their line lists.

A number of authors have cautioned against inappropriate modeling of HFS in stellar abundance analysis, either in terms of the use of inaccurate HFS atomic data or a complete absence of consideration for HFS. For example, Prochaska & McWilliam (2000) and Jofré et al. (2015b) found notable abundance systematics for certain elements (including V) arising from the suboptimal treatment of HFS. When presenting the Hypatia Catalog (a large compilation of detailed elemental abundance measurements for stars in the solar neighborhood), Hinkel et al. (2014) also commented on the increased scatter seen in literature abundances in elements such as Mn and V, speculating that a “casual” treatment of HFS could be to blame. On the other hand, several investigations have reached the broad conclusion that abundance measurements tend to be relatively insensitive to the inclusion of HFS (e.g., del Peloso et al. 2005; Takeda 2007; Hinkel et al. 2016; Jofré et al. 2017), which may appear to contradict the former set of studies. However, these latter works were mostly based on the analysis of a handful of elements in FG-type dwarfs over limited wavelength ranges, and their conclusions chiefly apply to the final results, which are averages over particular ensembles of chosen lines. For specific individual lines and, especially, for cooler stars, the latter studies have also noted significant HFS-related deviations.

Until very recently, elemental abundance studies have largely shunned M-type stars, as their cool temperatures promote the presence of molecules, giving rise to forests of poorly modeled lines that veil the continuum and distort atomic features. Elemental abundances other than iron have been characterized for only a handful of M dwarfs (Veyette et al. 2017; Souto et al. 2017, 2018; Abia et al. 2020; Ishikawa et al. 2020), mostly from high-resolution spectra in the *YJH* bands in the near-infrared (NIR) region ( $\lambda \gtrsim 960 - 1700$  nm). Unfortunately, in M dwarfs, the *YJH* bands host very few useful V lines. As a result, V abundance has been quantified for only one M dwarf, namely Kepler-138 (M1 V,  $T_{\text{eff}} \sim 3800$  K), using one line in the APOGEE *H* band ( $\lambda \sim 1592.4$  nm; Souto et al. 2017). More recently, Maldonado et al. (2020) determined abundances for a number of elements, including V, for  $\sim 200$  M dwarfs. Their approach was not based on the study of individual line profiles, but rather on broad features in severely degraded HARPS spectra ( $\sim 400-700$  nm,  $\mathcal{R} \sim 115\,000$  to  $\mathcal{R} \sim 1000-2000$ ). The features that best describe the degraded spectra were identified using principal component analysis, then correlated to abundances using a calibration sample of 19 FGK+M binaries. While their novel technique achieved impressive success for many of the elements considered, the V results presented in Maldonado et al. (2020) were dubious and significantly deviated from patterns measured for ensembles of FGK stars. Therefore, it appears that no robust analysis of vanadium on a large sample of M dwarfs has been performed yet.

Meanwhile, the CARMENES survey has provided high-resolution, high-quality spectra for hundreds of nearby M dwarfs. Some of these data were recently used to study rubidium, strontium, and zirconium in 57 local M dwarfs (Abia et al. 2020). In this present work, we focus on vanadium. In the wavelength region of 800 nm to 910 nm, which hosts a relatively low density of molecular lines, there exist about a dozen features of V I, many of them being extremely strong and prominently split by HFS. In some cases, the line shape deviations in these high-resolution spectra are so large that they are very far from being degenerate with any other conventional broadening parameters. We demonstrate that the striking vanadium line profiles seen in the CARMENES spectra can be excellently reproduced using the latest available atomic data and standard stellar models, assuming reasonable stellar parameters. From these features, we extracted robust vanadium abundances for 135 early M dwarfs and show that they track iron with little scatter, matching the patterns seen for local FG-type dwarfs.

This paper is organized as follows. Section 2.1 describes the CARMENES survey and the spectroscopic data products used for this work. Section 2.2 offers a heuristic description of the HFS-split vanadium features. We give an overview of HFS and its role in spectral modeling and abundance studies in Section 3. In Section 4, we document our effort to determine vanadium abundances for a subsample of early M dwarfs from the CARMENES survey. A comparison with the literature and discussion can be found in Section 5. In particular, the apparent overabundance of vanadium measured in some studies of K dwarfs is explored in Section 5.2, and Section 5.5 briefly examines the potential of vanadium abundance as a metallicity indicator for late-type stars. We give our conclusions in Section 6.

## 2. Vanadium lines in CARMENES spectra

### 2.1. The CARMENES survey

CARMENES is a spectroscopic survey of nearby M dwarfs to search for planets using the radial velocity method. The observations are conducted with the 3.5 m telescope at the Calar Alto Observatory in Almería, Spain, using the homonymous state-of-the-art fiber-fed high-resolution spectrograph with optical (VIS:  $\Delta\lambda \approx 520-960$  nm,  $\mathcal{R} \sim 94\,600$ ) and near-infrared (NIR:  $\Delta\lambda \approx 960-1710$  nm,  $\mathcal{R} \sim 80\,400$ ) channels (Quirrenbach et al. 2014, 2018). Since January 2016, the CARMENES project has collected high-quality spectra over multiple epochs of  $\sim 380$  stars across the full M-dwarf range as a part of its guaranteed time observations (GTO) program (Reiners et al. 2018; Schweitzer et al. 2019, hereafter Schw19). The utility of this data set has been demonstrated in numerous planet discoveries and atmospheric characterizations, as well as studies of stellar properties, such as activity and fundamental parameters (see Quirrenbach et al. 2020, for an overview)

As multiple spectra are taken over time for each target, they can be combined into a single “template spectrum” optimized for detailed stellar characterization, as follows: the raw spectra have been processed with the CARMENES pipeline *caracal*, which is based on flat-relative optimal extraction (Zechmeister et al. 2014) and wavelength calibration, which utilizes spectra from hollow cathode lamps and Fabry-Pérot etalons (Bauer et al. 2015). The spectra and, thus, the templates are corrected for telluric absorption following the template division telluric modeling approach (Nagel 2019), which employs *molecfit*<sup>1</sup> (Smette

<sup>1</sup> <http://www.eso.org/sci/software/pipelines/skytools/molecfit>

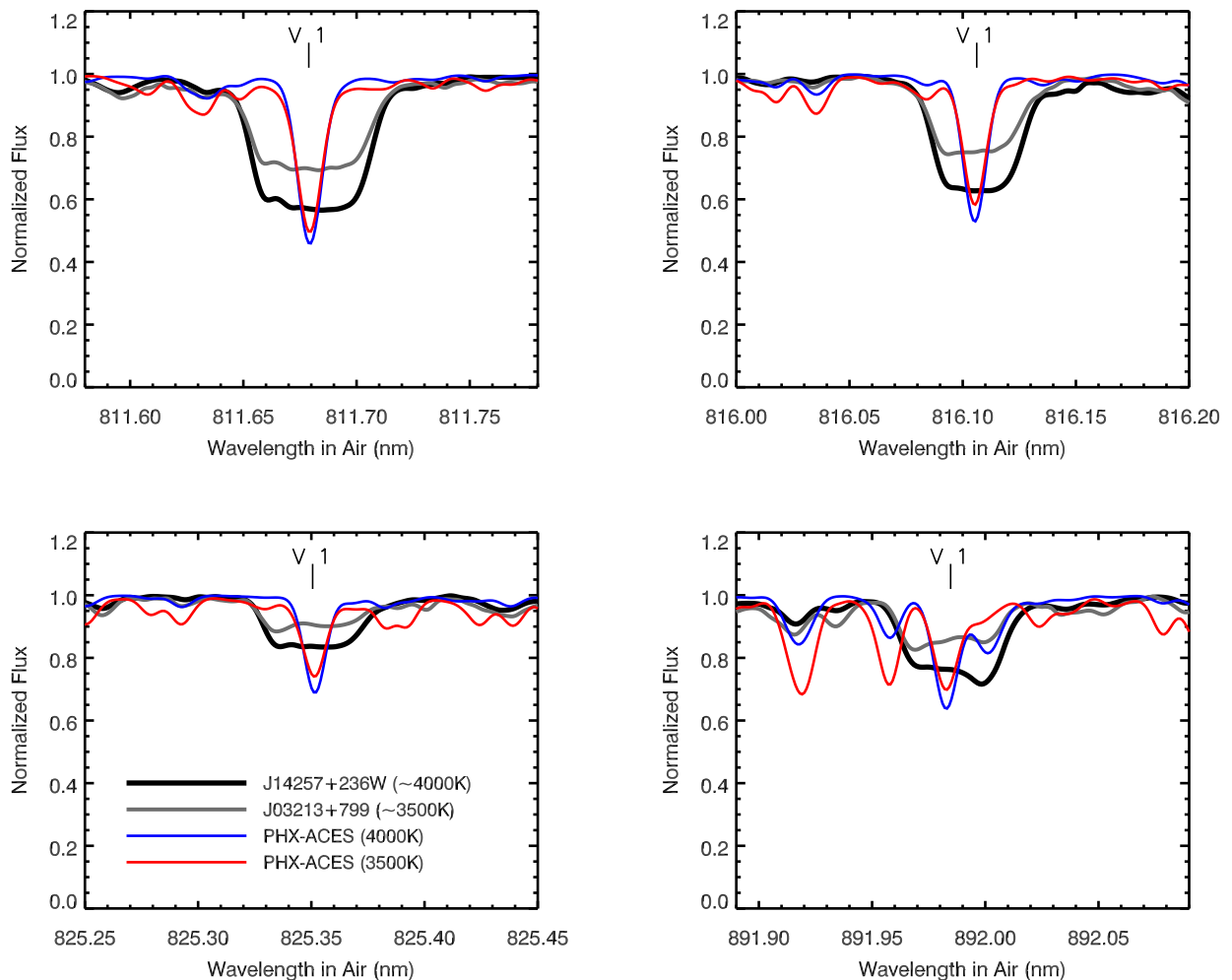


**Fig. 1.** Representative vanadium features in normalized, telluric absorption corrected, and co-added CARMENES spectra for M0.0 V (black, J14257+236W) and M2.0 V (gray, J03213+799) stars. Overplotted are PHOENIX-ACES spectra (1D LTE) convolved to the CARMENES instrumental resolution ( $\mathcal{R} = 94\,600$ ) for 4000 K (blue) and 3500 K (red) dwarfs for comparison. Wavelengths are given in terms of the rest frame as measured in air.

et al. 2015). In a further iteration, the *serval*<sup>2</sup> code (Zechmeister et al. 2018) coadds all spectra of each star via a B-spline regression and creates a telluric-free high S/N template spectrum (Caballero et al. 2016b). Each template spectrum, covering from 520 nm to 1710 nm with a few inter-order gaps mostly in the *H* band, comprises on average  $\sim 50$  individual spectra, and reaches S/N of  $> 100$  virtually throughout the entire wavelength range. The high resolution, high S/N, and virtual absence of telluric lines make these template spectra suitable for identifying and modeling fine features intrinsic to a given stellar spectrum.

## 2.2. Heuristic description of “square-bucket” features associated with $V_{\text{I}}$ lines

Compared to shorter wavelengths, the 800–910 nm region of M dwarf spectra is noticeably less impacted by molecular absorption in the stellar photosphere. After correction for telluric absorption, a series of features stand out in this wavelength range in the template spectra of many CARMENES GTO stars (see Fig. 1 for examples, and Figs. B.1 and B.2 for the whole 800–

910 nm region). These features are striking in appearance owing to their strength and breadth, and in particular their well-defined sharp corners, which cannot be reconciled with conventional broadening mechanisms of a single absorption line. Rather, each “bucket” resembles the smearing out of a forest of narrow, adjacent components. Some of these components are even marginally resolved into “wiggles”. These absorption profiles are ostensibly mismatched with synthetic spectra found in standard libraries (e.g., PHOENIX-ACES, Husser et al. 2013). Many of these features persist throughout the early M-dwarf range. They are associated with transitions of neutral vanadium atom.

The fact that these particular  $V_{\text{I}}$  transitions are affected by such substantial splitting in cool dwarfs may have received little attention because no previous program has conducted a dedicated M-dwarf survey at high resolution, with high S/N, and at multiple epochs so as to enable robust telluric corrections in the red optical wavelength range, as CARMENES has. The specific lines belonging to the  $V_{\text{I}}$  transitions that we consider here diminish in strength toward higher temperatures, nearly vanishing at about 5000 K, as most neutral vanadium becomes ionized (we note that  $V_{\text{II}}$  transitions also exist, but are extremely weak

<sup>2</sup> <https://github.com/mzechmeister/serval>

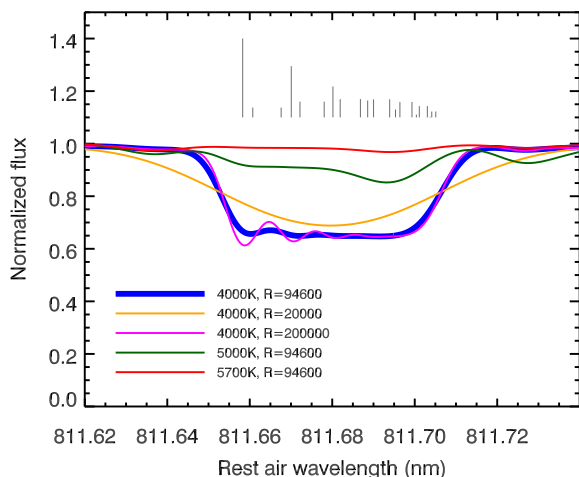


**Fig. 2.** Synthetic spectra around the dramatically split V I  $\lambda$ 811.7 nm synthesized by iSpec using the latest VALD3-HFS line list for solar vanadium abundance. This feature comprises 21 components, indicated by gray vertical lines whose heights scale with their expected relative strengths at  $T = 4000$  K, with EW used as a proxy for strength,  $\log(\text{EW}) = \log(gf\lambda) - \theta\chi$ , where  $\lambda$  is the transition wavelength in  $\text{\AA}$ ,  $\theta = 5040/T$ , temperature  $T$  is in K, and  $\chi$  is the lower excitation potential of the transition in eV. The strongest components toward the left side of the feature manifest themselves as marginally resolved “wiggles” in spectra with CARMENES-like resolution.

in M dwarfs in the optical wavelength range). These lines also lose their “corners” in lower resolution ( $R \sim 20\,000$ ) spectra (see Fig. 2). In cool dwarfs, many V I transitions are also visible at shorter wavelengths (e.g., 500–700 nm), but generally appear less broadened and significantly more blended with forests of molecular absorption.

### 3. Modeling the broad vanadium features with hyperfine structure

#### 3.1. Hyperfine splitting in stellar abundance studies

The broad V I features are a consequence of HFS splitting, a well-understood quantum effect arising from the interaction between electron angular momentum and nuclear magnetic moment, resulting in (typically) hyper-finely split energy levels within an atom (e.g., Condon & Shortley 1963; Sobelman 2006). HFS manifests itself in a number of atomic transitions, most notably in odd- $Z$  elements where an unpaired proton gives rise to a nonzero nuclear spin that, together with a large nuclear  $g$  factor, can result in a large nuclear magnetic moment. Besides V, other examples of prominent elements of astrophysical interest whose most common isotopes exhibit a high nuclear magnetic dipole moment include Mn, Co, Cu, Sc, Eu, and Rb. For these elements, failure to account for HFS could result in inadequately modeled line profiles and systematically incorrect abundances.

The importance of accurate HFS modeling in spectral analysis has gained recognition through works such as that of Prochaska & McWilliam (2000), who pointed out that incorrect HFS data for Mn and Sc had led to claims of spurious trends between abundances and metallicity and inappropriate conclusions about the mechanisms of Galactic nucleosynthesis (see also, e.g., Booth & Blackwell 1983; Vitas & Vince 2003; Bergemann et al. 2010; North et al. 2012; Jofré et al. 2019). HFS is now rou-

tinely incorporated in stellar abundance determinations of many elements. However, it has also been neglected in other notable studies (e.g., Feltzing & Gustafsson 1998; Neves et al. 2009; Adibekyan et al. 2012, but see Adibekyan et al. 2016 which does account for HFS). One reason for the lack of universal consideration is that, for many lines, the abundance biases introduced by neglecting HFS are minuscule because the shape distortions due to HFS are subtle and, for weak lines in the unsaturated regime, HFS preserves the equivalent widths. Another important obstacle in the way of accounting for HFS effects in spectral modeling might simply be the incompleteness or lack of accessibility to atomic data. The basic physics measurements required to characterize HFS patterns are not available for many split transitions and, even for those energy levels that have been measured, it is nontrivial to convert raw laboratory data into line information directly readable by standard software for atmosphere synthesis<sup>3</sup>. On the other hand, databases that do include HFS information tend to supply the HFS components in files separate from their default line lists (e.g., Kurucz 2011)<sup>4</sup>. This could hinder widespread usage, since it gives HFS an air of exoticism and requires extra initiative from the user to incorporate them into their studies.

The precise impact of unmodeled HFS on abundance measurements is correlated with line strength and depends strongly on the spectral type, the element, and the specific set of lines used in the analysis. However, the exact nature of these dependences is difficult to characterize, as the split patterns appearing for each transition are not simple functions of wavelength, temperature, or composite strength, and must be determined on a case-by-case basis. Several authors have investigated the magnitude of systematic errors introduced by neglecting HFS in FG- (and occasionally K-) type stars in the visual wavelength range for various elements, using small sets of lines (e.g., del Peloso et al. 2005; Takeda 2007; Jofré et al. 2015b, 2017; Hinkel et al. 2016). At least for the FG-type stars, the biases are often within typical uncertainties, especially when an abundance measurement is based on the mean over several lines. However, significant deviations were detected in specific individual lines, especially in strong lines toward the cool ends of the considered stellar samples. Empirically, the deviations were particularly evident in the works by Jofré et al. (2015b) and Jofré et al. (2017), where stars cooler than  $T_{\text{eff}} \lesssim 5000$  K like Arcturus were also studied. Therefore, to obtain accurate elemental abundance measurements for arbitrary types of stars, it is important to properly model all the HFS-affected lines whenever possible.

#### 3.2. Using HFS components for V I from the latest update in VALD3

HFS data have recently been added to the Vienna Atomic Line Database (VALD3), as detailed by Pakhomov et al. (2017, 2019). This supplementary database appears to be the result of an extensive effort to gather the latest atomic data from the literature, compute the associated HFS patterns, and output them into user-friendly forms. As of May 2020, these data have been readily accessible in the familiar format via the standard VALD3 web in-

<sup>3</sup> For a transition affected by HFS, laboratory data, if existent, are often given in terms of the magnetic dipole,  $A$ , and electric quadrupole,  $B$ , constants for the unsplit energy levels involved. Together with knowledge of the angular momentum quantum number,  $J$ , and nuclear spin,  $I$ , the HFS line component parameters can be computed via the Casimir formula and the Hönl-Kronig intensity rule (prescriptions described in, e.g., Woodgate 1980; McWilliam et al. 2013; Pakhomov et al. 2019).

<sup>4</sup> <http://kurucz.harvard.edu/linelists.html>

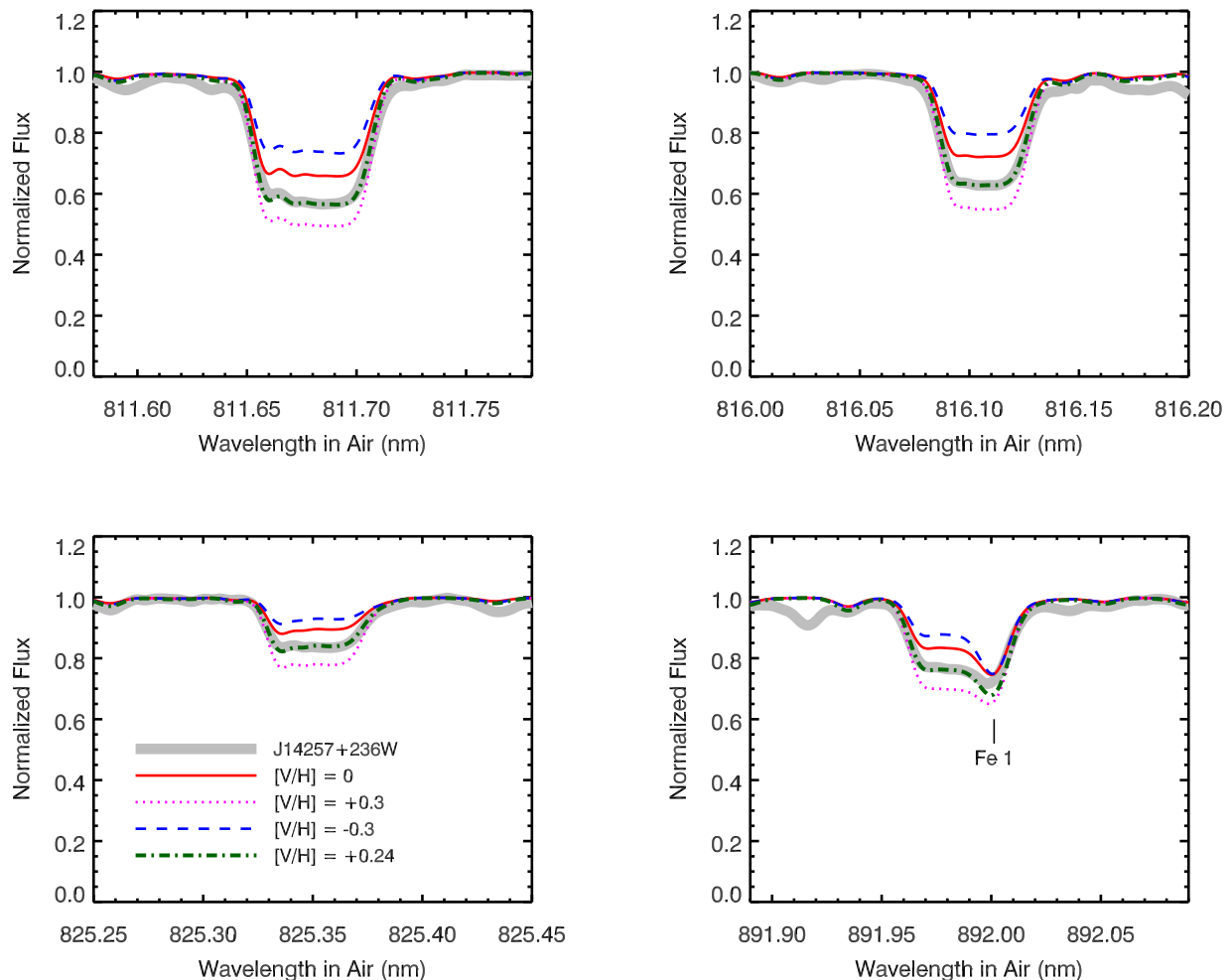


**Fig. 3.** Illustration of synthetic spectra generated with *iSpec* from the new VALD3 HFS atomic data for V compared with the CARMENES telluric-corrected composite spectrum of J14257+236W (gray) in several hyperfine-split V lines. Red solid, blue dashed, and magenta dotted lines are generic models with  $T_{\text{eff}} = 4000$  K,  $\log g = 4.5$ ,  $[M/H] = 0.0$ , and V abundances of solar (i.e.,  $A_{\odot}(\text{V}) = \log(N_{\text{V}}/N_{\text{H}})_{\odot} = -8.11$ , Asplund et al. 2009), +0.3 dex, and -0.3 dex. The best-matching model in green dash-dotted lines takes the basic stellar parameters from Schw19:  $T_{\text{eff}} = 4024$  K,  $\log g = 4.64$ ,  $[M/H] = +0.17$ , and  $A(\text{V}) = -7.87$  (i.e.,  $[V/H] = +0.24$ ), which simultaneously reproduces the overall shape of all the features. We note that the feature at 891.98 nm is blended with an Fe I line at 892.0 nm.

terface<sup>5</sup> by selecting the “HFS splitting” option. The atomic data collection for vanadium therein includes, among others, recent results from the Wisconsin atomic group (Lawler et al. 2014; Den Hartog et al. 2014; Wood et al. 2014).

We downloaded and converted these line lists into a format recognized by the stellar spectroscopy software package *iSpec* (Blanco-Cuaresma et al. 2014; Blanco-Cuaresma 2019). Using *iSpec*, we simulated a number of broad vanadium features between 800 nm and 910 nm, seen in the CARMENES VIS spectra. With the settings described in Sect. 4.3 and 4.6, we generated model spectra that satisfactorily reproduce the observed prominent V I line profiles in early M dwarfs, an example of which is shown in Fig. 3. The depths of the features appear to exhibit a high sensitivity to the exact V abundance value assumed. By tweaking the V abundance in the synthetic spectra, excellent matches can be made simultaneously by the model to all the features that we considered, suggesting the potential effectiveness

of these features for abundance determination using the spectral synthesis technique.

#### 4. Measuring vanadium abundances of cool stars

The presence of strong and modelable vanadium features in a relatively clean region of cool star spectra points to an opportunity to characterize V abundances of all stars of similar type. We used spectral synthesis fits to derive vanadium abundances for a large number of early M dwarfs in the CARMENES GTO sample.

##### 4.1. Atomic data

We used the “extract stellar” option of the VALD3 web interface to download a list of all line data, including HFS-split-line components, in the vicinity of the regions defined in Table 1 with theoretical depth exceeding  $10^{-3}$  for 4000 K and 3500 K dwarf stars. The 4000 K line list was used for stars with  $T_{\text{eff}} \gtrsim 3700$  K and the 3500 K line list was for those with  $T_{\text{eff}} \lesssim 3700$  K. These

<sup>5</sup> <http://vald.astro.uu.se>

**Table 1.** Wavelength regions used for the V abundance fits.

$\lambda_{\text{central}}$ (nm)	$\lambda_{\text{low}}$ (nm)	$\lambda_{\text{upp}}$ (nm)	# comps. modeled <sup>a</sup>	$T_{\text{eff}} \gtrsim$ 3700 K	$T_{\text{eff}} \lesssim$ 3700 K
802.7366	802.70	802.90	18	yes	yes
809.3468	809.32	809.37	12	yes	yes
811.6789	811.64	811.72	21	yes	yes
814.4560	814.44	814.47	6	yes	yes
816.1062	816.06	816.15	16	yes	yes
818.6728	818.63	818.70	10	yes	no
824.1599	824.13	824.17	6	yes	yes
825.3506	825.30	825.39	18	yes	yes
825.5896	825.56	825.61	12	yes	yes
891.9847	891.95	892.02	18	yes	yes
893.2947	893.26	893.34	12	yes	no
903.7613	903.74	903.79	4	yes	no
904.6693	904.64	904.70	10	yes	no

Notes: <sup>a</sup>: Number of HFS components included in the line model.

line lists include all atomic species, as well as several molecules including TiO, MgH, CH, CO, C<sub>2</sub>, OH, and CN.

#### 4.2. Line region selection

Through systematic visual inspection of V  $\iota$  lines in the M-dwarf spectra at 800–910 nm, we identified 13 regions that are well modeled using the new VALD3 atomic line lists for stars around 4000 K. For stars with  $T_{\text{eff}}$  closer to 3500 K, where molecular contamination becomes more significant, there are nine such regions for which the profile match quality is tolerable. Therefore, in choosing the set of lines to fit, we made a distinction between earlier- ( $T_{\text{eff}} \gtrsim 3700$  K) and later- ( $T_{\text{eff}} \lesssim 3700$  K) type M dwarfs. Overall, our selected line regions have a variety of strengths and breadths attributed to HFS, and are potentially suitable for V abundance determination. These regions and the number of split components that compose them are listed in Table 1 and illustrated in Figs. C.1 and C.2. We note that the line regions with fewer split components tend to look less “square”.

#### 4.3. Synthetic spectra and fitting algorithm

As described in Section 3.2, we used the *iSpec* stellar spectroscopy software to synthesize and fit model spectra generated from the new line lists. *iSpec* is a highly versatile program developed for stellar parameter and abundance analysis. It allows users to mix and match suites of atmosphere structure grids and radiative transfer codes (Blanco-Cuaresma 2019), and comes preloaded with several popular options of both. The user provides the program with a solar elemental abundance pattern and line lists in the wavelength regions under consideration. Then, given a set of stellar properties ( $T_{\text{eff}}$ ,  $\log g$ ,  $[M/H]$ ,  $\alpha$ ), broadening parameters ( $v_{\text{mic}}$ ,  $v_{\text{mac}}$ ,  $v \sin i$ , instrumental resolution) and individual abundances, *iSpec* can synthesize the stellar spectra by interpolating the atmosphere structure grid. It can also perform the inverse problem, deriving fundamental parameters and abundances from an input spectrum and line region definitions, using either SSF (based on an iterative  $\chi^2$  minimization algorithm) or EW. The continuum model can be found by fitting splines to a

version of the spectra smoothed with maximum and median filters, as described by Blanco-Cuaresma et al. (2014) and Blanco-Cuaresma (2019). The spline and window parameters are specified by the user. For broadening, *iSpec* uses a radial-tangential kernel for macroturbulence and the standard Gray kernel for rotation (Gray 1992). For comparison with observed spectra, the synthesized spectra are convolved with a Gaussian line profile corresponding to the user-specified resolution of instrument. For all of our analyses, we chose the MARCS 1D, plane-parallel, LTE atmosphere models (Gustafsson et al. 2008) paired with the radiative transfer code *Turbospectrum* version 15.1 (Plez 2012), both as provided in *iSpec*. Our solar abundance pattern followed Asplund et al. (2009). We used the *iSpec* SSF scripts to perform line-by-line fits to the applicable V  $\iota$  line regions, varying only V abundance and fixing all other fit parameters to those externally determined or assumed. Where only  $[Fe/H]$  is available (e.g., in the literature), we take it as a proxy for  $[M/H]$ , *iSpec*’s scaling factor for the overall elemental abundance pattern ( $[M/H]$  is a measure of the average overall metal content, which is expected to deviate from  $[Fe/H]$ , the iron abundance, at low metallicities, mainly due to an enhancement of  $\alpha$ -elements. However, the distinction between  $[Fe/H]$  and  $[M/H]$  is sometimes casually treated in the M dwarf literature, meaning that some published  $[Fe/H]$  values may be closer to  $[M/H]$  – see Marfil et al. 2021 for a relevant discussion).

#### 4.4. Test case: Arcturus

Arcturus is a K giant with publicly-accessible, high-resolution ( $R \sim 150\,000$ ), high signal-to-noise ( $S/N \sim 1000$ ) échelle spectra across the entire optical wavelength range (373–930 nm, Hinkle et al. 2000). It is also the only late-type star with V abundance exquisitely measured from 55 lines at optical wavelengths (550–910 nm) with a complete accounting of the most up-to-date knowledge of the atomic parameters and HFS effects (Wood et al. 2018). This makes Arcturus a suitable benchmark target on which to test our method. Our independent selection of line regions turns out to be very similar to those used by Wood et al. (2018) in the 800–910 nm range. We excluded the V  $\iota$   $\lambda 897.1673$  nm and  $\lambda 908.5231$  nm lines because they appear to be affected by relatively heavy molecular blending in early M-dwarf spectra.

Where possible, we adopted identical stellar parameters as used in the analysis of Wood et al. 2018:  $T_{\text{eff}} = 4275$  K,  $\log g = 1.3$ ,  $v_{\text{mic}} = 1.6$  km s<sup>-1</sup>, and  $[Fe/H] = -0.55$  dex, taken from Peterson et al. (2017). In addition, we fixed  $v \sin i = 1.5$  km s<sup>-1</sup> and  $v_{\text{mac}} = 5.2$  km s<sup>-1</sup>, as measured by Gray & Brown (2006) for Arcturus. The fitted synthetic spectra were convolved to  $R = 150\,000$  using a Gaussian profile to match the resolution of the Arcturus spectrum. We used *iSpec*’s default continuum settings whereby quadratic B-splines were fitted to 5 nm segments filtered using the “median+max” scheme, where the median filter was 0.05 nm and the maximum filter was 1.0 nm wide. We performed line-by-line fits to the 13 lines listed in Table 1, arriving at  $\langle \log \epsilon(V) \rangle = 3.55 \pm 0.01$  (sample standard deviation  $\sigma = 0.04$ )<sup>6</sup>. Our value compares very well with the determination by Wood et al. (2018) of  $\langle \log \epsilon(V) \rangle = 3.54 \pm 0.01$  from 55 lines ( $\sigma = 0.04$ ).

<sup>6</sup>  $\log \epsilon(X) \equiv \log_{10}(N_X/N_H) + 12$ .

#### 4.5. CARMENES sample selection

We visually inspected the telluric-corrected template spectra of 331 CARMENES GTO targets to identify stars that prominently exhibit the V HFS features of interest and in which these features can be adequately reproduced by the models. We observed that spectra of M dwarfs with  $T_{\text{eff}} \lesssim 3400$  K tend to be very contaminated in a majority of the lines and surrounding continuum regions that we considered (from Section 4.2), whereas those with  $T_{\text{eff}} \gtrsim 3500$  K and  $v \sin i < 4$  km s<sup>-1</sup> are well-fit in most of the line regions under consideration. Based on the  $T_{\text{eff}}$  determined for this sample from Schw19 whenever possible and, otherwise, from Passegger et al. (2019) and Passegger et al. (2018), we removed 117 stars with  $T_{\text{eff}} < 3400$  K. A further 34 stars had no measured  $T_{\text{eff}}$  in any of the references given above because they are fast rotators, are very late-type stars, or have an S/N that is too low. Therefore, we discarded those as well. Of the 117 stars with  $T_{\text{eff}} > 3500$  K, we retained all except J16102–193, which has a  $v \sin i = 7.3$  km s<sup>-1</sup> (Reiners et al. 2018), J11201–104 and J18174+483, which show large broadening in the V features in excess to that accountable by the measured  $v \sin i$ , J00162+198W and J05532+242, which are double-lined spectroscopic binaries (Baroch et al. 2018), J15474–108, which is a spectroscopic triple (Baroch et al. 2021), and J04219+213, which exhibits large spurious features. This left 110 stars. In the remaining sample of 63 stars with  $3400 \text{ K} \leq T_{\text{eff}} \leq 3500 \text{ K}$  we first eliminated four stars that have a measured  $v \sin i > 4$  km s<sup>-1</sup>, leaving 59 stars. We assessed these by eye and picked out a further 25 stars where a majority of the features appear to be fit decently with the model spectra. The resulting sample consisted of  $110 + 25 = 135$  early M dwarfs, all of which have  $T_{\text{eff}} \gtrsim 3400$  K and  $v \sin i < 4$  km s<sup>-1</sup>.

#### 4.6. Vanadium abundances for the CARMENES GTO subsample

We fit to the V regions as listed in Table 1 for this subsample of early M dwarfs from the CARMENES GTO program<sup>7</sup>. In these fits, the stellar parameters  $T_{\text{eff}}$ ,  $\log g$ , and  $[\text{Fe}/\text{H}]$  were fixed to those derived by Schw19 based on PHOENIX-ACES model fits to metal lines in the same spectra. iSpec picks an atmosphere structure model consistent with the expected  $\alpha$  enhancement as a function of  $[\text{M}/\text{H}]$  through the usual relation ( $[\alpha/\text{Fe}] = 0.0$  for  $[\text{M}/\text{H}] = 0.0$ , increasing to  $+0.4$  for  $[\text{M}/\text{H}] = -1.0$ ; Gustafsson et al. 2008). Since macroturbulence velocities,  $v_{\text{mac}}$ , are not well-characterized for cool dwarfs, but are likely to be small (e.g., extrapolation from Fig. 17.10 in Gray 1992 extends below  $1$  km s<sup>-1</sup> for stars later than K3 V – see also Lindgren et al. 2016), we set the  $v_{\text{mac}}$  parameter to  $1.0$  km s<sup>-1</sup> in our fits. The microturbulence velocity  $v_{\text{mic}}$  is determined by iSpec’s built-in function and depends on  $T_{\text{eff}}$ ,  $\log g$ , and  $[\text{M}/\text{H}]$ . For M dwarfs,  $v_{\text{mic}}$  as assigned by iSpec is generally between  $0.8$  km s<sup>-1</sup> and  $0.9$  km s<sup>-1</sup>. The values recommended by Husser et al. (2013) based on convective velocities from the PHOENIX-ACES models are approximately  $v_{\text{mic}} \sim 0.5$  km s<sup>-1</sup>. We checked that the final fit results are insensitive to such small  $v_{\text{mic}}$  variations. Where possible, we used the  $v \sin i$  values measured by Reiners et al. (2018) for this sample. When only an upper limit of  $2$  km s<sup>-1</sup> is available, we set  $v \sin i = 2$  km s<sup>-1</sup>. We convolved the synthesized spectra with a

<sup>7</sup> The following V I lines were excluded from the fit for the following objects: J12248–182:  $\lambda 825.3506$  nm (too weak); J14082+805:  $\lambda 816.1062$  nm (contaminated); J16167+672S:  $\lambda 818.6728$  nm and  $\lambda 825.3506$  nm (contaminated); J17355+616:  $\lambda 818.6728$  nm (contaminated).

Gaussian instrumental line profile corresponding to the resolving power of the CARMENES VIS spectrograph. As in the Arcturus fit, the local continuum normalization was done using the “median+max” scheme with window length of  $0.05$  nm and  $1.0$  nm respectively.

The high-S/N input template spectra are already shifted into the rest frame with wavelength given in air, with the velocity shift determined from the fitted peak of a cross-correlation function with the PHOENIX-ACES spectra for the corresponding stellar parameters. Therefore, in all our abundance fits, the radial velocity ( $v_r$ ) was set to  $0$  km s<sup>-1</sup>.

We present the mean V abundances derived from our individual line-by-line fits in Table A.1, given in terms of  $[\text{V}/\text{H}]$ <sup>8</sup>. Figure 4 shows the V-to-Fe abundance ratio of this sample as a function of metallicity (i.e.,  $[\text{Fe}/\text{H}]$  from Schw19). Since the  $[\text{V}/\text{Fe}]$  value is not directly constrained in our fits, we calculated it as  $[\text{V}/\text{H}] - [\text{Fe}/\text{H}]$ . Our  $[\text{V}/\text{Fe}]$  values lie close to  $0.00$  dex (sample standard deviation =  $0.09$  dex), consistent with that of FG-type stars in the solar neighborhood (e.g., Battistini & Bensby 2015, hereafter BB15). The later-type stars in the sample (i.e.,  $T_{\text{eff}} < 3700$  K) present a larger scatter than the earlier-type stars (i.e.,  $T_{\text{eff}} > 3700$  K). This could be a consequence of cooler star V abundances being more sensitive to metallicity errors (see Section 4.7) and systematically poorer line fits (see Section 4.8).

#### 4.7. Error quantification

One standard way to estimate the error in abundance measurements is through the line-to-line scatter. Column  $\delta[\text{V}/\text{H}]$  in Table A.1 lists the sample standard deviation of the line abundances over all the lines considered for each star. This is typically  $0.03$  dex to  $0.07$  dex (typically  $\sim 0.04$  dex for  $T_{\text{eff}} > 3700$  K and  $\sim 0.06$  dex for  $T_{\text{eff}} < 3700$  K, see also Fig. 5). The standard error of the mean (SEM) line abundances (sample standard deviation over square root of the number of lines) is another commonly used measure of abundance error. For all but two stars in our sample, the SEM lies between  $0.01$  dex and  $0.03$  dex.

Errors in  $[\text{V}/\text{H}]$  arising from uncertainties in the input stellar parameters were calculated for two representative stars and listed in Table 2. To derive these values, we varied the  $T_{\text{eff}}$ ,  $\log g$ , and  $[\text{Fe}/\text{H}]$  one-by-one within their formal  $1\sigma$  errors as given by Schw19 ( $51$  K,  $0.07$  dex, and  $0.16$  dex, respectively). The total expected errors contributed by the uncertainty of stellar parameters is calculated from summing each source of error in quadrature (i.e., they are treated independently from one another). Adding the line-to-line standard deviations,  $0.06$  dex and  $0.08$  dex are representative total uncertainties in our V measurements for typical M0.0 V and M2.0 V stars, respectively.

#### 4.8. Line-to-line abundance systematics

We now examine the quality of the line selections and how our final abundance results depend on them. In Fig. 5 we plot the deviations of individual line abundances from the mean over all lines for the whole sample. On the whole, the abundances derived from our choice of lines show decent agreement. The scatter is typically within  $\pm 0.05$  dex, which is comparable to or better than that of similar studies. However, in every line there exists various degrees of systematic deviation, in general worsening for cooler stars. The largest differences are found in the V I

<sup>8</sup> We used the standard definition  $[\text{X}/\text{H}] \equiv \log \epsilon(\text{X}) - \log \epsilon_{\odot}(\text{X})$ , where  $\log \epsilon(\text{X}) \equiv \log_{10}(N_{\text{X}}/N_{\text{H}}) + 12$  and  $\log \epsilon_{\odot}(\text{V}) = 3.93$  (Asplund et al. 2009).

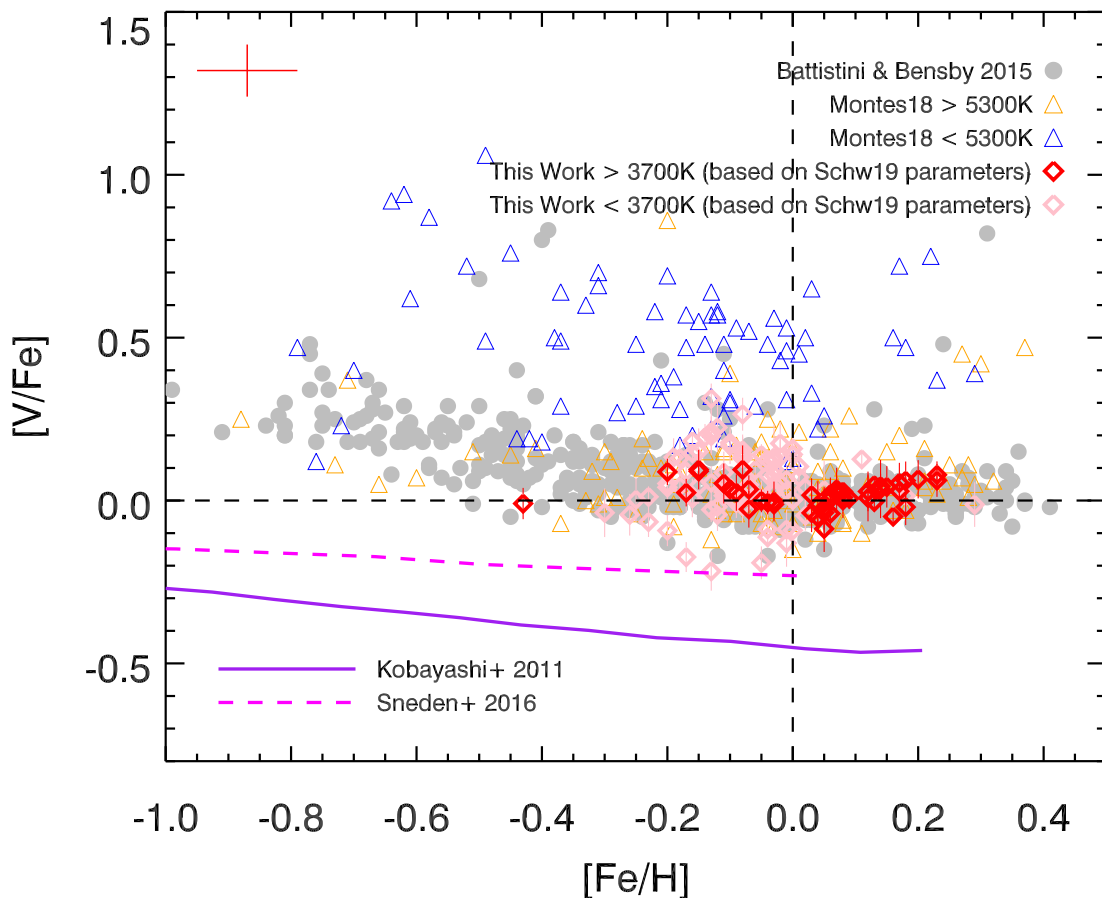


**Fig. 4.** [V/Fe] versus [Fe/H] diagram of the 135 CARMENES GTO stars derived from our line-by-line analysis (red diamonds for  $T_{\text{eff}} > 3700$  K and pink diamonds for  $T_{\text{eff}} < 3700$  K). Each vertical error bar represents the sample standard deviation of the abundances derived from the set of V lines used for each star. The typical error in the literature metallicity used in our analysis is 0.16 dex (Schw19), also shown in the upper left of the figure. Overplotted are selected representative V measurements in populations of nearby FGK stars from the literature. Gray filled circles are measurements from Battistini & Bensby (2015) for local FG dwarfs. The triangles show results from Montes et al. (2018) for local FGK dwarfs, with blue denoting the K-dwarf subsample therein ( $T_{\text{eff}} < 5300$  K). The V abundances measured for these K dwarfs are generally significantly higher than for the rest of the stars, possibly a consequence of not having accounted for HFS in the modeling. The purple line shows the predicted trend for the solar neighborhood from the Galactic chemical evolution models of Kobayashi et al. (2011). The dashed magenta line shows a model from Sneden et al. (2016), which is built upon the Kobayashi et al. (2011) model but incorporates a hypernova jet effect.

**Table 2.** Abundance sensitivity to uncertainties in stellar parameters (from Schw19) for two representative stars in the sample.

Stellar parameters	J14257+236W ( $T_{\text{eff}} \sim 4000$ K)	J03213+799 ( $T_{\text{eff}} \sim 3500$ K)
$T_{\text{eff}} \pm 51$ K	$\pm 0.01$ dex	$\pm 0.02$ dex
$\log g \pm 0.07$ dex	$\pm 0.03$ dex	$\pm 0.02$ dex
$[\text{Fe}/\text{H}] \pm 0.16$ dex	$\pm 0.03$ dex	$\pm 0.05$ dex
Total	0.04 dex	0.06 dex

fect the accuracy of the modeling by introducing line blending or complicating the determination of the pseudo-continuum level, as well as make the fits more sensitive to uncertainties in metallicity. The V  $\lambda 814.4560$  nm,  $\lambda 816.1062$  nm,  $\lambda 825.3506$  nm, and  $\lambda 825.5896$  nm lines show good agreement with the average at temperatures higher than  $\sim 3700$  K, but fare more poorly for cooler stars. This is again indicative of inadequate modeling of molecules. The presence of systematic abundance discrepancies from line to line calls for caution in interpreting abundance constraints from single or small sets of lines unless they are very well-understood.

$\lambda 818.6728$  nm,  $\lambda 824.1599$  nm, and  $\lambda 891.9847$  nm lines. Abundances derived from these lines are on average 0.05 dex above or below the mean across all lines, and can differ more severely for individual stars. As shown in Figure C.2, these line regions are more contaminated by molecules and Fe I lines, which could af-

Examples of single lines that could potentially be used effectively on their own are the V  $\lambda 809.3468$  nm and  $\lambda 811.6789$  nm lines. Both appear to trace the mean abundance very well and exhibit very little scatter. The fact that they are useful throughout the  $T_{\text{eff}}$  range of 3400 K to 4200 K makes them the most dependable single V abundance indicator lines in this wavelength and



temperature range. By extension, they could be promising metallicity proxies as well (see Section 5.5).

#### 4.9. Fits using alternative stellar parameters

Accurate determination of M-dwarf stellar parameters is an active area of research and method-dependent disagreements are commonplace. There is some evidence that the existing published metallicity values for the CARMENES GTO stars (Passegger et al. 2018, 2019, Schw19) derived from PHOENIX model grid fits predominantly to strong Fe, Ti, Mg, and K lines in the optical and NIR, may be somewhat systematically overestimated. For Passegger et al. (2019), who used the latest PHOENIX-SESAM model grids, the systematic offset is especially evident for the earliest M dwarfs and most metal-poor stars (also see a literature comparison in Figs. 5 and 6 of Passegger et al. 2019). The problem is less severe, but possibly still persists, for the parameters given by Schw19, which were based on PHOENIX-ACES grids. For example, the apparent dearth of relatively metal-poor stars ( $[\text{Fe}/\text{H}] < -0.3$ ) in the sample could be suggestive of metallicity measurements being biased to higher values. A detailed investigation of such deviations is beyond the scope of this paper. It may be a combination of saturation effects in the lines, spectral model inadequacies, the neglect of  $\alpha$  enhancement, NLTE effects, or something else (see also Abia et al. 2020; Ishikawa et al. 2020; Olander et al. 2021, for discussions). Therefore, it is worthwhile to check the robustness of our V abundances to alternative sets of stellar parameters.

One further effort to re-determine the fundamental stellar parameters uniformly for the entire CARMENES GTO sample will be presented in a forthcoming publication by Marfil et al. (2021), using the spectral analysis software SteParSyn (Tabernero et al. 2018, 2021). SteParSyn is an automatic code designed to infer the stellar atmospheric parameters  $T_{\text{eff}}$ ,  $\log g$ ,  $[\text{Fe}/\text{H}]^9$ , and  $v \sin i$  of late-type stars (FGKM) following the spectral synthesis method using a Markov Chain Monte Carlo algorithm. This code has already been used in spectroscopic studies that involve late FGKM stars in a variety of astrophysical scenarios (e.g., Tabernero et al. 2018; Palle et al. 2021; Borsa et al. 2021). The work of Marfil et al. (2021) is based on a synthetic spectral grid generated from BT-Settl model atmospheres (Allard et al. 2012) coupled to Turbospectrum (Plez 2012) in a large number of Fe I and Ti I line regions, as well as TiO bandheads. Currently, some of the  $\log g$  values determined with SteParSyn appear to be possibly too large. Therefore, for our work, we assigned new  $\log g$  values based on  $T_{\text{eff}}$  and  $[\text{Fe}/\text{H}]$  via the PARSEC isochrones (Bressan et al. 2012; Chen et al. 2014), similar to the procedure used by Passegger et al. (2019). The isochrone model inputs were the fitted  $T_{\text{eff}}$  and  $[\text{Fe}/\text{H}]$  from Marfil et al. (2021), and age estimates as given by Passegger et al. (2019). We present the SteParSyn-derived  $T_{\text{eff}}$  and  $[\text{Fe}/\text{H}]$ , as well as the  $\log g$  constrained from the isochrones, for our CARMENES GTO subsample in Table A.1. For simplicity, we refer to this collection of alternative stellar parameters, consisting of  $T_{\text{eff}}$  and  $[\text{Fe}/\text{H}]$  from Marfil et al. (2021) and the modified  $\log(g)$ 's, as the ‘‘Marfil+’’ values.

As shown in Fig. 6, the metallicities given in Marfil+ and in Schw19 systematically differ. The discrepancy is largest for relatively metal-poor stars, which also tend to be cooler: those deemed by SteParSyn to have  $[\text{Fe}/\text{H}] < -0.2$  have on average 0.19 dex higher value according to Schw19. Another puzzling pattern is that the majority of stars with super-solar metallicities

according to Schw19 are part of the warmer ( $> 3700$  K) subset, while the metal-poor stars according to Marfil+ are almost exclusively cooler ( $< 3700$  K). These discrepancies are discussed in more detail by Marfil et al. (2021).

Despite the large systematic differences, the final derived  $[\text{V}/\text{H}]$  abundances assuming each set of stellar parameters are very similar. Figure 7 compares the  $[\text{V}/\text{H}]$  values determined from line-by-line fits where  $T_{\text{eff}}$ ,  $\log g$ , and  $[\text{Fe}/\text{H}]$  were fixed to the Marfil+ values with those based on the Schw19 values. Although there is a small systematic offset of 0.034 dex overall (0.056 dex for the metal-poor stars with  $[\text{Fe}/\text{H}] < -0.2$ ), the agreement is within 0.10 dex in the vast majority of cases, even when the  $[\text{Fe}/\text{H}]$ s differ by up to  $\sim 0.4$  dex. The relative insensitivity of V abundance derived from the lines used in this work to the exact stellar parameters is not surprising given the error analysis presented in Section 4.7. Therefore, in spite of systematic uncertainties in the exact stellar parameters, our  $[\text{V}/\text{H}]$  values (relative to the solar V abundance of Asplund et al. 2009) could be taken as robust.

Finally, we show  $[\text{V}/\text{Fe}]$  versus  $[\text{Fe}/\text{H}]$  for the Marfil+ stellar parameters in Figure 8, which exhibits overall good agreement with the distribution of stars from BB15. Since the fitted  $[\text{V}/\text{H}]$  values for the two sets of stellar parameters are very similar, the qualitative differences between Fig. 8 and Fig. 4 chiefly reflect the differing metallicity measurements between Schw19 and Marfil+. One curious dissimilarity concerns the relative scatter in  $[\text{V}/\text{Fe}]$  between the cooler and warmer subsets: the notably smaller  $[\text{V}/\text{Fe}]$  scatter in the warmer stars in Fig. 4 is not reproduced in Fig. 8. These patterns could arise from a complex interplay between the errors from the line fits, systematic uncertainties in the stellar parameters, and perhaps also astrophysical causes. Disentangling these factors is beyond the scope of this work.

## 5. Discussion

### 5.1. Comparison with local FG dwarfs and K giants

The  $[\text{V}/\text{Fe}]$  versus  $[\text{Fe}/\text{H}]$  trend for the local CARMENES M-dwarf sample is consistent with the behavior observed in populations of local Galactic disk FG-dwarfs stars (e.g., BB15) for the overlapping metallicity range ( $-0.6$  dex to  $+0.3$  dex), as shown in Figs. 4 and 8. BB15 performed a comprehensive study of odd-Z iron peak element abundance in the solar neighborhood. In particular, they carried out a large spectroscopic study of 714 FG-dwarfs (Bensby et al. 2014), 466 of which have a measured  $\log \epsilon(\text{V})$ . The analysis was done using a line-by-line approach and differentially with respect to the Sun. The authors modeled HFS effects in five V I line regions between 550 nm and 630 nm, taking the line component data from Prochaska et al. (2000). An abundance is considered by the authors to be determined if at least one of the five lines appears to be well fit. The BB15 results are also largely compatible with other large studies of nearby stars that have accounted for HFS, including the NIR spectroscopic study of K giants in the SDSS-APOGEE survey of Hawkins et al. (2016) and the local giant sample of Lomaeva et al. (2019).

### 5.2. A potential partial solution to the issue of abundance-temperature relation in local K dwarfs

A number of well-known abundance studies whose samples also included K dwarfs, many of them dealing with distinguishing the chemical compositions of planet hosts from barren stars, no-

<sup>9</sup> Denoted as  $[\text{Fe}/\text{H}]_{\text{corr}}$  in Marfil et al. (2021).

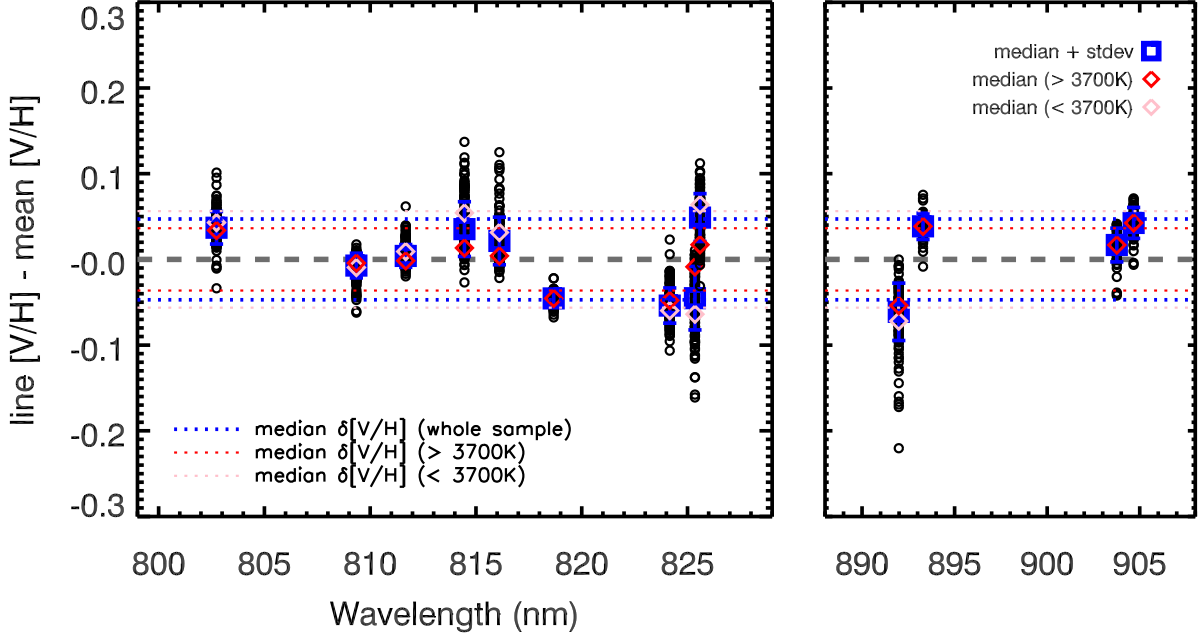


**Fig. 5.** Individual line abundance deviations from the mean abundance across the lines for the star sample. At each given line wavelength (in air), the black circles denote the line  $[V/H] - \text{mean } [V/H]$  for each star in which that line was studied. The thick orange squares show the median abundance deviation and sample standard deviation for each line (over all the CARMENES stars for which that line was used). The blue and red squares mark the same metric for the warmer ( $T_{\text{eff}} > 3700$  K) and cooler ( $T_{\text{eff}} < 3700$  K) subsamples, respectively. The horizontal dotted lines bracket the median abundance error (in terms of the line-to-line standard deviation) for the whole sample ( $\pm 0.047$  dex, blue squares), the warmer subsample ( $\pm 0.036$  dex, red diamonds), and the cooler subsample ( $\pm 0.056$  dex, pink diamonds). The  $V \text{ I } \lambda 818.6728$  nm,  $\lambda 893.2947$  nm,  $\lambda 903.7613$  nm, and  $\lambda 904.6693$  nm lines were not fitted for stars with  $T_{\text{eff}} < 3700$  K.

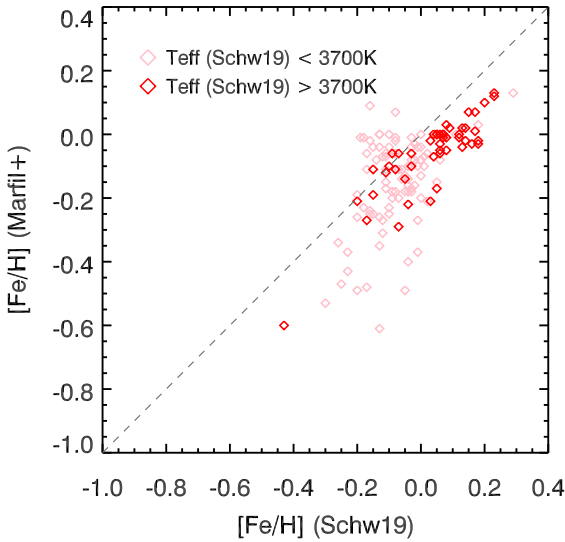


**Fig. 6.** Comparison between  $[Fe/H]$  from Schw19 and Marfil+. The pink and red diamonds denote stars with  $T_{\text{eff}} < 3700$  K and  $T_{\text{eff}} > 3700$  K, respectively. The thin gray dashed line is the one-to-one line.

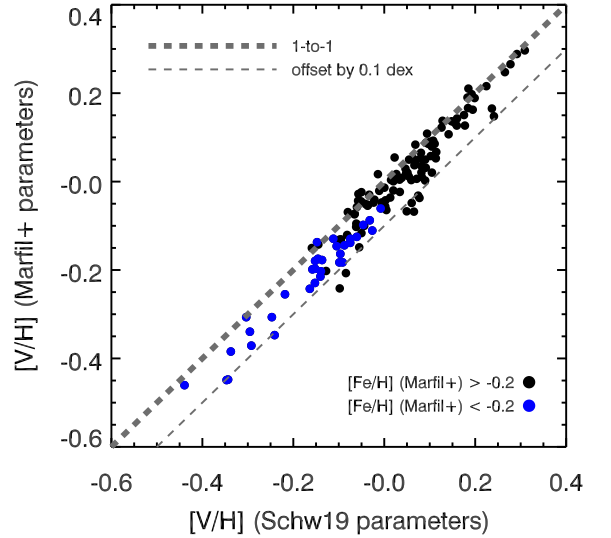


**Fig. 7.**  $[V/H]$  measured with stellar parameters fixed to those from Marfil+ versus Schw19. Black and blue points denote stars with  $[Fe/H] > -0.2$  and  $[Fe/H] < -0.2$ , respectively. The thick and thin gray dashed lines mark the one-to-one line and that offset by 0.1 dex.

ticed a puzzling systematic trend with regard to V abundance. For example, in a sample of about 1000 FGK stars, Adibekyan et al. 2012 (hereafter AD12) measured  $[V/Fe]$  of around 0.0 dex throughout the FG spectral type range, but rising steadily from 0.0 dex to +0.6 dex as  $T_{\text{eff}}$  decreases from 5300 K to 4500 K

(as shown in Fig. 10). Incidentally, a similar trend is observed therein for Sc, another element known to exhibit HFS (see Section 3). Recognizing it to be unphysical, the authors attributed this behavior to a variety of possible causes, including increased

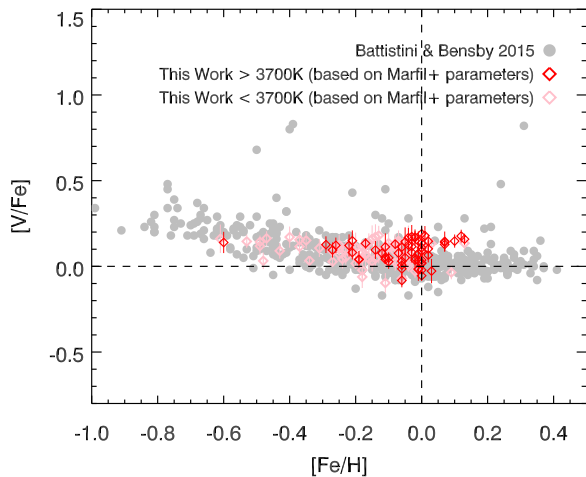


**Fig. 8.** Same as Fig. 4, but for fits based on the Marfil+ stellar parameters for 135 stars. The vertical error bars represent the sample standard deviation of the line-to-line abundances.

line blending for cool stars, NLTE, inaccurate model atmosphere structures, and imprecise  $\log(gf)$  values.

Larger scatter and a systematic correlation with  $T_{\text{eff}}$  below 5300 K was also observed in, for example, Bodagheer et al. 2003; Gilli et al. 2006; Neves et al. 2009; Tabernero et al. 2012; Jofré et al. 2015a, and Montes et al. 2018, prompting some authors to either empirically correct the measurements in this temperature range, or to disregard them altogether. This trend is weaker but still visible in the sample of GK-type giants of Adibekyan et al. (2015). In Fig. 4, we overplot the results of Montes et al. (2018), who measured elemental abundances for FGK-type dwarfs in multiple systems with M-dwarf common proper motion companions. The distribution of  $[V/Fe]$  for stars with  $T_{\text{eff}} > 5300$  K and  $T_{\text{eff}} < 5300$  K are far removed from each other, with those below 5300 K enhanced by more than  $\sim +0.5$  dex on average compared to solar.

The oscillator strengths for many V I transitions were improved by Lawler et al. (2014), which could impact works that used older line lists. However, many of the aforementioned analyses were conducted differential with respect to the Sun and, therefore, uncertainties in  $\log(gf)$  are expected to cancel. More interesting is the fact that none of the works that found an abundance-temperature trend appear to have used HFS components in their spectral analysis. Inspired by our present work with V lines in cool dwarfs, we hypothesized that a failure to account for HFS could be a key factor responsible for the apparent V overabundance in K dwarfs. Indeed, HFS was already proposed as a possible reason for the large scatter in  $[V/Fe]$  of nearby stars compiled from the literature in the Hypatia Catalog (Hinkel et al. 2014). A hint could also be found in the work of Maldonado et al. (2015), who also determined elemental abundances in FGK stars. The line regions used in that work for the V analysis were identical to those of Adibekyan et al. (2012), but Maldonado et al. (2015) included HFS components for the subset of V I lines redward of 600 nm (Ramírez et al. 2014). The temperature dependence below 5300 K was still somewhat visible, but far less severe.

To investigate our hypothesis within our existing analysis framework, we performed a simple experiment. We simulated G- and K-dwarf spectra in the V I line regions used in the abun-

dance work of AD12 with iSpec. We did this once with the new HFS components, to mimic reality, and once with an older line list likely resembling what would have been used in the previous analysis, to mimic past methodologies. The line profiles are compared in Fig. 9 for a K dwarf  $T_{\text{eff}} = 4800$  K,  $\log g = 4.4$ ,  $[M/H] = 0.0$  dex,  $v \sin i = 1.0$  km s $^{-1}$ , and  $v_{\text{mic}} = 1.0$  km s $^{-1}$ , and for a G dwarf with  $T_{\text{eff}} = 5700$  K,  $\log g = 4.4$ ,  $[M/H] = 0.0$  dex,  $v \sin i = 1.05$  km s $^{-1}$ , and  $v_{\text{mic}} = 3.92$  km s $^{-1}$ . The first thing to note is that, unlike the bucket-shaped lines presented in this work, these line shapes are visually not markedly different from Gaussian and, therefore, they may not raise a red flag. Another thing to note is that all the lines in the K dwarf indeed appear broader (and in some cases also deeper) when HFS is taken into account. Though the effect is subtler in some lines than others, large deviations are apparent for V I  $\lambda 573.7062$  nm,  $\lambda 573.7062$  nm, and  $\lambda 625.1823$  nm. On the other hand, deviations are almost invisible across all the lines in the G dwarf. A third point is that these lines at K dwarf temperatures,  $T_{\text{eff}} \approx 4800$  K, are much stronger than in G dwarfs and, therefore, more likely to be affected by saturation, which would mean HFS would no longer conserve their EWs.

To quantify the impact of the difference between expected and actual line profiles on abundance measurements, we performed line-by-line synthetic spectral fits to the mock spectra generated using HFS components on a temperature grid from 4500 K to 5500 K in increments of 100 K. All mock spectra were synthesized with solar metallicity,  $\log g = 4.6$  for  $T_{\text{eff}} \leq 5000$  K and  $\log g = 4.5$  for  $T_{\text{eff}} > 5000$  K, and  $v_{\text{mic}} = 0.88$  km s $^{-1}$  to  $0.98$  km s $^{-1}$ , with  $v_{\text{mac}}$  and  $v \sin i$  set to 0. The models used for the abundance fits were generated with a line list ignoring HFS. We ran a trial retrieval using the most current  $\log(gf)$  values from Lawler et al. (2014). In addition, we repeated the trials with the  $\log(gf)$  data used by Neves et al. (2009) (Table 2 therein), which are systematically lower than the updated values by about 10%. In all the fits, only the V abundance was allowed to vary. We took the mean of the abundances retrieved from the seven lines and used the standard error of the mean as an indication of measurement error. Figure 10 overplots the simulated  $[V/Fe]$  versus  $T_{\text{eff}}$  on the results from AD12.

The upward trend with decreasing temperature starting from 5300 K is reproduced by our simulations with a very similar slope and inflection point. Moreover, the worsening line-to-line scatter seen in AD12 also quantitatively resembles that of our simulation. A few “bad” lines have a big impact. Exchanging the outdated oscillator strengths with the new values results in a systematic offset of 0.05 dex to 0.10 dex, although this difference should only manifest when considering abundance retrievals on an absolute scale. The remaining offset suggests that other sources of systematics still need to be identified, for example NLTE effects or stellar model differences. While no dedicated NLTE study of neutral vanadium has been conducted to date, systematic differences between abundances derived from V II versus V I lines in metal-poor stars do hint that NLTE might be important (Ou et al. 2020). It has also been suggested that, at least in Sun-like photospheres, NLTE effects may be significant in V I due to the majority of V atoms being in the singly-ionized state (Scott et al. 2015). The shape and magnitude of the deviation pattern may also differ when using an EW method, as was done by AD12 and similar works. Nevertheless, the results from our simulated SSF abundance retrievals indicate that failure to take HFS into account could play a key role in introducing artificial trends and enhancing the measured V abundances of K dwarfs.

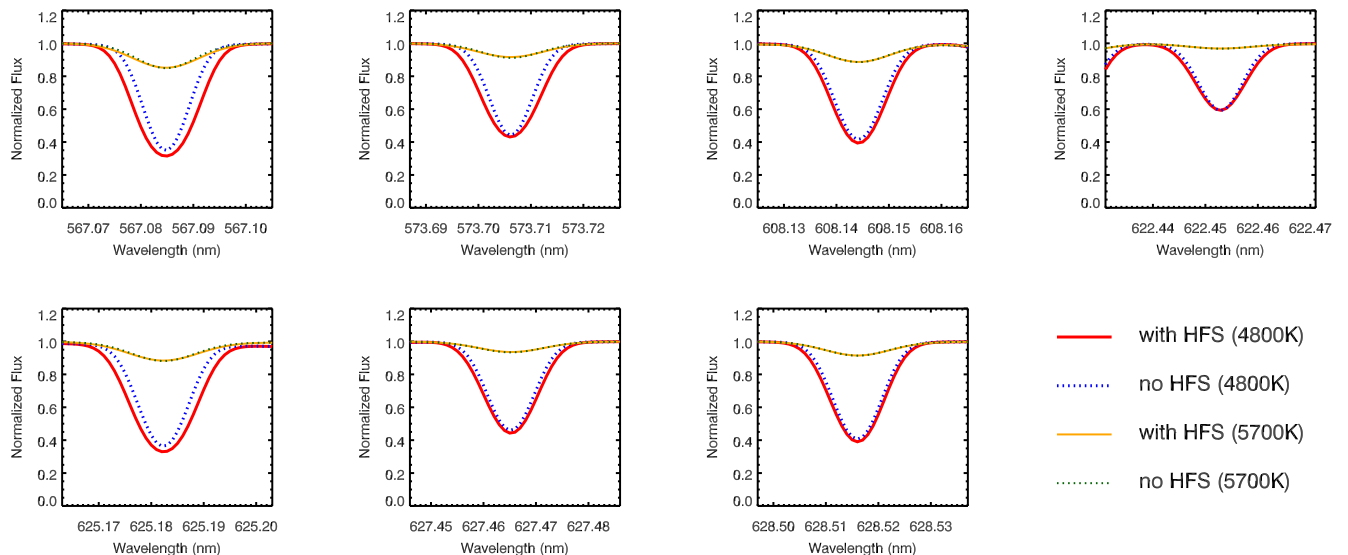


**Fig. 9.** Comparison of simulated profiles of vanadium lines used in Adibekyan et al. (2012), without and with HFS components, for a K dwarf ( $T_{\text{eff}} = 4800$  K) and a G dwarf ( $T_{\text{eff}} = 5700$  K) with a solar abundance pattern at CARMENES VIS resolution ( $R \sim 94\,600$ ). The red and orange solid lines are generated from the VALD3 atomic line list including the latest HFS components, for the K and G dwarf respectively. The dotted blue and green lines are simulated from a line list without HFS components. The lines are much stronger in later-type stars. While most lines show very small deviations, a few lines (notably  $\lambda 567.085$  nm,  $\lambda 573.707$  nm, and  $\lambda 625.183$  nm) in the K dwarf exhibit significant systematic differences when HFS is considered.

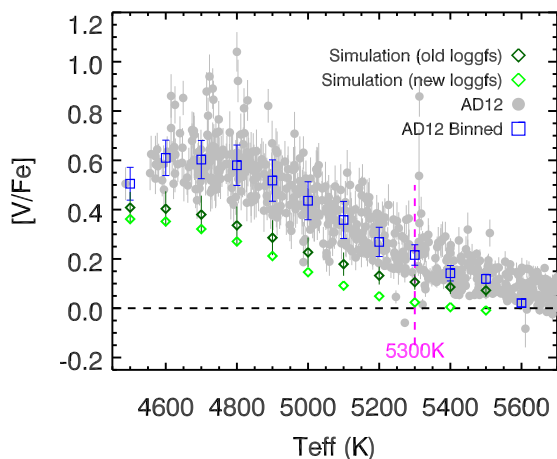


**Fig. 10.** Vanadium abundances based on line-by-line synthetic spectral fitting analysis without HFS on mock spectra generated with an HFS line list as a function of temperature, compared to the abundance trend in AD12. The gray filled circles are measurements and error (computed as line-to-line  $\text{RMS}/\sqrt{7}$  for seven lines) by AD12 and the blue squares show the median of these measurements and error binned by temperature. The dark green diamonds show the mock retrieval results for model spectra with  $\log(gf)$  values from Neves et al. (2009) for the V lines, whereas the light green diamonds use the latest  $\log gf$  values. Below 5300 K, the “measured”  $[V/Fe]$  increases with decreasing effective temperature in a very similar manner as found by Adibekyan et al. (2012) and others. The observed line-to-line scatter as a function of  $T_{\text{eff}}$  also resembles the simulated behavior.

The effect of unmodeled HFS on vanadium abundance measurements in Sun-like stars was already identified in the appendix of Takeda (2007). They quantified the expected system-

atic abundance bias from the EW method for nine V I lines between 560 nm and 660 nm, two of which are in common with the lines we examined (see Fig. 15 therein). They also found significant corrections to be required for individual lines such as the one at 567.084 nm, especially at large strengths. Takeda (2007)’s final conclusion that this correction is “insignificantly small” (i.e.,  $\leq 0.05$  dex when averaged over all nine lines) seemingly contradicts our findings. However, considering that their study was limited to cases where  $T_{\text{eff}} \geq 5000$  K, the results of Takeda (2007) are actually quite compatible with ours. An extrapolation of the steepening trend of the correction factor with  $T_{\text{eff}}$  below  $T_{\text{eff}} = 5000$  K (in their Fig. 16) would imply much larger offsets at cooler temperatures. Further discrepancies could also arise from differences in the exact choice of lines. Relatedly, for red clump giants ( $4400 \text{ K} < T_{\text{eff}} < 5100 \text{ K}$ ), Liu et al. (2007) demonstrated that HFS introduced up to +0.5 dex of bias in V abundances derived from the three lines that they considered ( $\lambda 567.0854$  nm,  $\lambda 572.7057$  nm,  $\lambda 621.6358$  nm). The deviation worsens with increasing metallicity, presumably because the magnitude of the correction tends to grow with line strength.

### 5.3. Trends within the thin and thick disks

The literature is divided on the existence and nature of fundamental differences in V abundance trends as a function of Galactic population. In a study of ten thick-disk stars, Prochaska et al. (2000) measured an enhancement of about +0.2 dex in  $[V/Fe]$  over solar, which is notably higher than the typical  $[V/Fe]$  measurements for thin disk stars available at the time. However, using the same atomic data, Brewer & Carney (2006) found no significant distinction between V abundance patterns of 23 G dwarfs in the thin and thick disk. Combining data from Reddy et al. (2003), Reddy et al. (2006) leveraged  $\sim 360$  nearby thin- and thick-disk FG stars to find a  $\sim 0.1$  dex offset between the distribution of  $[V/Fe]$  for the thick disk over the thin disk. With 466 FG dwarfs, BB15 showed that  $[V/Fe]$  of disk stars

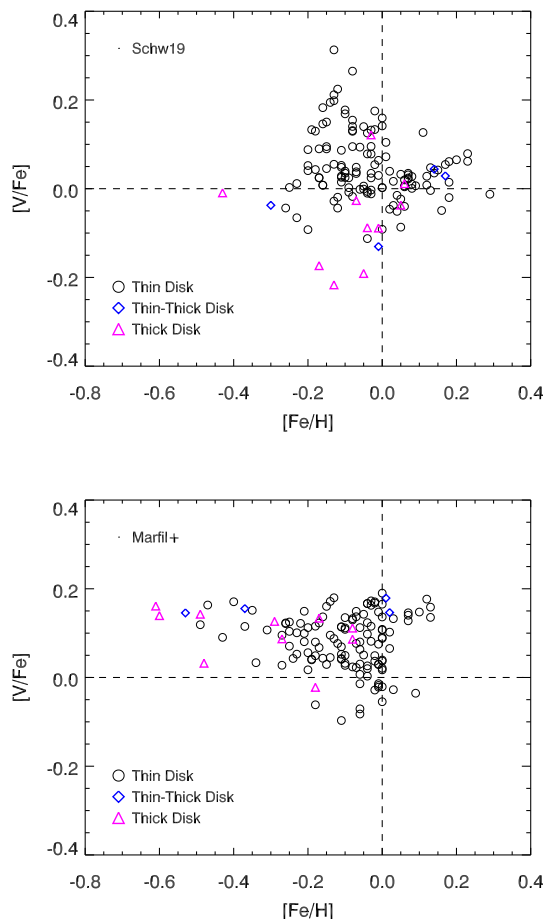


**Fig. 11.**  $[V/Fe]$  versus  $[Fe/H]$  of the 135 CARMENES-GTO stars derived from our line-by-line analysis, color- and symbol-coded for their membership attribution to Galactic kinematic groups (CC21). Top: analysis based on stellar parameters from Schw19. Bottom: analysis based on stellar parameters from Marfil+. The thick-disk members appear to be better distinguished in metallicity space with the parameters estimated by Marfil+.

in their sample is mostly flat around solar with a slight uptick at the lower end of its metallicity range, whereas a more pronounced sloped relationship of decreasing metallicity and increasing  $[V/Fe]$  emerges for the thick disk. While the two segments are visually dissimilar, the authors argued that the thick disk is merely a continuous extension of the thin disk trend into lower metallicities. Recently, Lomaeva et al. (2019) resolved a clear,  $\sim 0.1$  dex parallel separation between trends in  $[V/Fe]$  versus Fe abundance for  $\sim 300$  giant stars belonging to the thin and thick disk (see Fig. 3 therein), even for overlapping metallicity ranges between  $-0.4$  dex and  $-0.1$  dex. We note that the criteria for disk membership assignment are not uniform across the studies. For example, in BB15, the classification was made using isochronal age (with the thin-thick disk boundary drawn at 7–9 Gyr), while Lomaeva et al. (2019) assigned stars to the thin or thick disk based on its  $[Fe/H]$ ,  $[Ti/Fe]$ , and Galactic kinematics.

Using kinematic designations from the Carmencita catalog (Caballero et al. 2016a; Cortés-Contreras 2017), we investigate whether there are thin/thick disk distinctions in V abundance trends in this sample, as shown in Fig. 11. We mark three different kinematic categories: the thin disk, the thick disk, and the

thin-thick disk (i.e., stars with intermediate characteristics, as defined by Montes et al. 2001). While the Marfil+  $[Fe/H]$  values appear to be better correlated with the kinematic designations than the Schw19 metallicities, we are unable to identify a meaningful trend using either sets of stellar parameters. This could partially be due to small number statistics. All but 14 out of the 135 stars studied here belong to the thin disk.

#### 5.4. Implication for Galactic nucleosynthesis

Our measurements reinforce the disagreement between observational and theoretical expectations from GCE models, which predict a significantly lower vanadium-to-iron abundance ratio across this metallicity range. Overplotted on Fig. 4 are the relations between  $[V/Fe]$  and  $[Fe/H]$  in the solar neighborhood from the GCE model of Kobayashi et al. (2011) and its variant presented in Sneden et al. (2016). The Kobayashi et al. (2011) model is calculated from the then-updated theoretical nucleosynthetic yields for SNe types Ia and II (including hypernovae), as well as for asymptotic giant branch (AGB) stars, in conjunction with observationally constrained initial mass functions (IMFs) and star formation history (SFH) models. The predicted vanadium abundance is around  $-0.5$  dex below that observed for a large range of stellar types and metallicities. Similar deficiencies are also present for Sc and Ti (Kobayashi et al. 2011; Nomoto et al. 2013). In addition to the need to better understand SNe explosion parameters and yields, proposed physics solutions include possible production enhancement facilitated by neutrino interactions (Kobayashi et al. 2011), the use of multidimensional nucleosynthetic models (Nomoto et al. 2013), incorporation of hypernovae jet effects (Sneden et al. 2016), and revised parameters for the IMF and assumptions for SFH and Galaxy formation scenarios (Sneden et al. 2016). The Sneden et al. (2016) model shown in Fig. 4 is based on the Kobayashi et al. (2011) model and includes bipolar jets from hypernovae in addition, which reduces the tension with observation to  $< 0.3$  dex. Despite hints of progress, no model to date has satisfactorily reproduced the observed trend. Our work further highlights persistent problems with the current understanding of nucleosynthesis mechanisms and supernova yields for vanadium in the context of the Milky Way’s formation history.

#### 5.5. Potential as a metallicity indicator in cool stars

Traditionally, M-dwarf spectra have the notoriety of being riddled with multifarious mysteries (e.g., molecules, magnetic fields, mismatched features). As models grow more sophisticated and data become more exquisite, the question of spectroscopic metallicities for M dwarfs has become the subject of many investigations over the past decade. While many avenues (i.e., spectral ranges and stellar models) have been explored, and progress has been made, modern high-resolution studies still struggle to agree on metallicities for individual cool stars (e.g., Veyette et al. 2017; Passegger et al. 2018, 2019; Souto et al. 2020; Sarmiento et al. 2021) and are also in tension with low-resolution counterparts (e.g., Rojas-Ayala et al. 2012; Mann et al. 2013; Newton et al. 2014). Among other implications, the question of metallicity has a significant impact for exoplanet demographics studies (e.g., Fischer & Valenti 2005; Johnson et al. 2010; Buchhave et al. 2014; Petigura et al. 2018).

Above  $[Fe/H] \sim -0.5$  dex, V appears to trace Fe abundance in lockstep in a large variety of settings (e.g., Feltzing & Gustafsson 1998; Battistini & Bensby 2015; Erandes et al. 2018), with

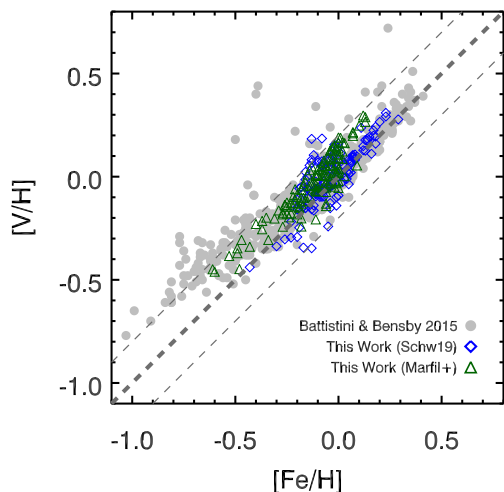


**Fig. 12.**  $[V/H]$  versus  $[Fe/H]$  measured for stars in the solar neighborhood. The thick gray dashed line is the one-to-one line, while the thin gray dashed lines bracket the  $\pm 0.2$  dex regions. In this metallicity range,  $[V/H]$  appears to correlate tightly with  $[Fe/H]$ , reflecting its potential as an alternative metallicity indicator.

dispersion on the order of 0.1 dex. Figure 12 shows that  $[V/H]$  versus  $[Fe/H]$  for ours and the BB15 sample of stars in the solar neighborhood fall largely within 0.2 dex to the one-to-one line. Below  $[Fe/H] \sim -0.5$  dex,  $[V/H]$  deviates from an exact correspondence, but maintains a linear correlation with  $[Fe/H]$ . In both regimes, the scatter is comparable to or better than precisions currently achievable for metallicity measurements for M dwarfs as well as study-to-study variations for individual stars. Furthermore, we have demonstrated in Section 4 that  $[V/H]$  can be easily and robustly determined nearly independently of other fundamental stellar parameters. Even for cases where a large discrepancy exists between the  $[Fe/H]$ s inferred by different procedures (up to  $\sim 0.4$  dex), the measured  $[V/H]$ s agree within 0.1 dex. Therefore, methods described in this work could represent an alternative, indirect way to estimate the metallicity for M dwarfs. A growing number of high-resolution spectrographs (e.g., 2.2 m La Silla-FEROS, VLT-UVES, Keck-HIRES, Lick-Hamilton, Gemini-MAROON-X, NEID, HET-HPF, LBT-PEPSI) cover the wavelength range considered in this work. Analyses using observations from these instruments should be capable of delivering reliable vanadium measurements and potentially metallicity proxies for M dwarfs.

## 5.6. Implications for planets

### 5.6.1. Planet hosts

To date, 19 of the stars in our sample are known planet hosts. As shown in Fig. 13, the  $[V/H]$  distribution of known planet hosts and non-planet hosts do not appear to be significantly different. This is not surprising, as most of the planets hosted by our stars are Neptune-sized or smaller, for which a notable correlation between occurrence rate and the detailed chemical composition of the host star is not expected (e.g., Adibekyan et al. 2012).

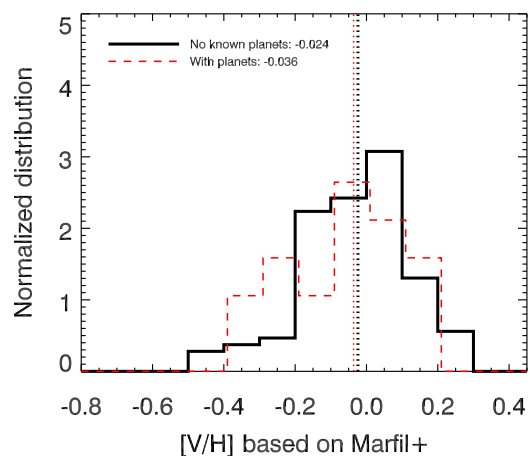
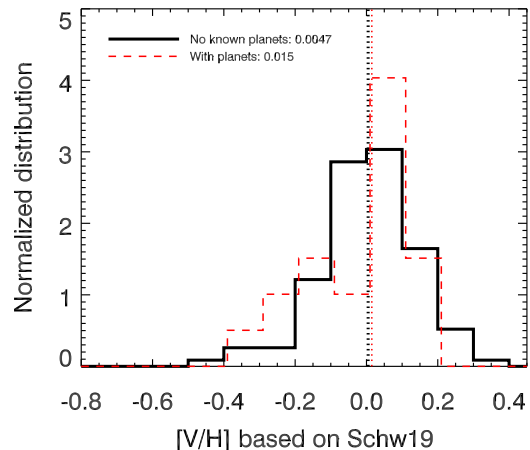


**Fig. 13.** Normalized distributions of  $[V/H]$  for known planet hosts (red) versus the rest of the stars (black) in the sample based on stellar parameters from Schw19 (*top*) and Marfil+ (*bottom*). The medians of each distribution are marked by the vertical dotted lines and given in the legends.

### 5.6.2. Planetary atmospheres

As better and more precise spectrographs are being developed at large aperture telescopes, V and other atomic species can be searched for in planetary atmospheres. In fact, V has already been detected in at least one planetary atmosphere (WASP-121b Borsa et al. 2021; Ben-Yami et al. 2020). HFS does not seem to pose a problem for the detection of individual lines in transmission spectroscopy, as the analyses are centered on the stronger lines, and the lines are typically broadened in the planetary atmospheres. However, the use of an HFS line list in the calculation of atomic cross-sections could affect the S/N of the signals. Future studies dealing with retrieving atmospheric abundances of exoplanets might have to take this effect into account.

It is also interesting to consider how the effect of HFS might manifest in molecules such as VO. While VO, TiO, and metallic species such as Fe II are believed to be responsible for the thermal inversion of hot exoplanet atmospheres (Yan et al. 2020), there is still no clear detection of VO in a planetary atmosphere. Given that the detection of VO relies on the cross-correlation technique (Snellen 2004), where hundreds of VO spectral lines

are cross-correlated to a template, perhaps such methods are more sensitive to HFS effects. However, since the effect of HFS in molecules is more difficult to characterize, and does not appear to be well-studied for VO, a detailed exploration of this topic is beyond the scope of this paper.

## 6. Conclusion

Detailed chemical analysis for cool stars stands at the cusp of exploration. In this work, we have performed one of the first elemental abundance studies for a large sample of M dwarfs. In the high-resolution, high S/N, telluric-corrected CARMENES spectra, we located about a dozen hyperfine-split atomic V I lines in the 800–910 nm region, which have clear presentations and are relatively free of molecular contamination. Using the latest hyperfine components for V I from VALD, we have shown that these lines can be modeled well and that they are sensitive to abundances and relatively insensitive to uncertainties in other fundamental stellar parameters. Using spectral synthesis fits to these line regions, we obtained robust [V/H] measurements for 135 nearby, early M dwarfs ( $T_{\text{eff}} > 3400$  K) in the CARMENES GTO sample, with typical errors of  $\sim 0.07$  dex. The [V/Fe] versus [Fe/H] trend closely resembles that observed for local FG-type stars, lying significantly above predictions from GCE models based on the current knowledge of Galactic star formation history and nucleosynthesis channels for this element. Moreover, the tight correlation between Fe- and V- abundances in nearby stars and the relative ease to measure photospheric [V/H] in high-resolution cool star spectra suggests that V has the potential to be an effective metallicity indicator for local M dwarfs.

We have discussed at length the risks of not properly accounting for HFS, which could bias abundance measurements in various ways. A number of large stellar abundance surveys have reported a systematic trend of increasing [V/Fe] with decreasing  $T_{\text{eff}}$  for K dwarfs ( $T_{\text{eff}} \lesssim 5300$  K). Through simple toy simulations, we have shown that the neglect of HFS is likely responsible for this phenomenon to a large extent. However, the exact impact of HFS on abundance measurements cannot be generalized, as the degree of splitting depends on the exact atomic transition parameters of the lines considered and the properties of the atmosphere. The amount of correction required must be evaluated on a case-by-case basis by considering the stellar type and exact set of lines involved. The safest course of action in any abundance analysis is to use only lines that are well understood (i.e., have complete atomic data available), whenever possible, and to fully model this effect.

Our investigation underlines the fact that HFS can have a dramatic impact on line profiles and on abundance measurements. We suggest that this quantum effect could play an important role in cool star spectroscopy where a number of elements appear to exhibit stronger and wider splitting patterns than in Sun-like stars. We have exploited this property to provide a reasonable assessment of V abundance in the cool photospheres of the most abundant type of stars in the Galaxy. This type of study is made possible with the accessibility of constantly improving laboratory measurements, which are essential and powerful tools for interpreting increasingly complex stellar spectra in new temperature and wavelength regimes. Together with Abia et al. (2020) for Rb, Sr, and Zr, and other forthcoming papers, our findings in the CARMENES spectra open new windows for elemental analysis in cool stars.

*Acknowledgements.* We thank Nikola Vitas and Andrew McWilliam for pedagogical discussions on the nature of HFS splitting. We are grateful to our referee Vardan Adibekyan for insightful feedback that helped to improve the

quality of this manuscript. CARMENES is an instrument at the Centro Astronómico Hispano-Alemán (CAHA) at Calar Alto (Almería, Spain), operated jointly by the Junta de Andalucía and the Instituto de Astrofísica de Andalucía (CSIC). CARMENES was funded by the Max-Planck-Gesellschaft (MPG), the Consejo Superior de Investigaciones Científicas (CSIC), the Ministerio de Economía y Competitividad (MINECO) and the European Regional Development Fund (ERDF) through projects FICTS-2011-02, ICTS-2017-07-CAHA-4, and CAHA16-CE-3978, and the members of the CARMENES Consortium (Max-Planck-Institut für Astronomie, Instituto de Astrofísica de Andalucía, Landessternwarte Königstuhl, Institut de Ciències de l'Espai, Institut für Astrophysik Göttingen, Universidad Complutense de Madrid, Thüringer Landessternwarte Tautenburg, Instituto de Astrofísica de Canarias, Hamburger Sternwarte, Centro de Astrobiología and Centro Astronómico Hispano-Alemán), with additional contributions by the MINECO, the Deutsche Forschungsgemeinschaft (DFG) through the Major Research Instrumentation Programme and Research Unit FOR2544 “Blue Planets around Red Stars”, the Klaus Tschira Stiftung, the states of Baden-Württemberg and Niedersachsen, and by the Junta de Andalucía. We acknowledge financial support from the Agencia Estatal de Investigación of the Ministerio de Ciencia, Innovación y Universidades and the ERDF through projects PID2019-109522GB-C51[1:4]/AEI/10.13039/501100011033 and the Centre of Excellence “Severo Ochoa” and “María de Maeztu” awards to the Instituto de Astrofísica de Canarias (CEX2019-000920-S), Instituto de Astrofísica de Andalucía (SEV-2017-0709), and Centro de Astrobiología (MDM-2017-0737), the Generalitat de Catalunya/CERCA programme, the Austrian Science Fund (P 33140-N), the Ministerio de Universidades (FPU15/01476), the DFG (SPP 1992 JE 701/5-1), and NASA (NNX17AG24G). This work has made use of the VALD database, operated at Uppsala University, the Institute of Astronomy RAS in Moscow, and the University of Vienna.

## References

- Abia, C., Taberner, H. M., Korotin, S. A., et al. 2020, *A&A*, 642, A227  
 Abt, A. 1952, *ApJ*, 115, 199  
 Adibekyan, V., Delgado-Mena, E., Figueira, P., et al. 2016, *A&A*, 592, A87  
 Adibekyan, V., Dorn, C., Sousa, S. G., et al. 2021, arXiv e-prints, arXiv:2102.12444  
 Adibekyan, V. Z., Benamati, L., Santos, N. C., et al. 2015, *MNRAS*, 450, 1900  
 Adibekyan, V. Z., Sousa, S. G., Santos, N. C., et al. 2012, *A&A*, 545, A32  
 Allard, F., Homeier, D., & Freytag, B. 2012, *Philosophical Transactions of the Royal Society of London Series A*, 370, 2765  
 Allende Prieto, C. 2016, *Living Reviews in Solar Physics*, 13, 1  
 Asplund, M., Grevesse, N., Sauval, A. J., & Scott, P. 2009, *ARA&A*, 47, 481  
 Baroch, D., Morales, J. C., Ribas, I., et al. 2021, arXiv e-prints, arXiv:2105.14770  
 Baroch, D., Morales, J. C., Ribas, I., et al. 2018, *A&A*, 619, A32  
 Battistini, C. & Bensby, T. 2015, *A&A*, 577, A9  
 Bauer, F. F., Zechmeister, M., & Reiners, A. 2015, *A&A*, 581, A117  
 Ben-Yami, M., Madhusudhan, N., Cabot, S. H. C., et al. 2020, *ApJ*, 897, L5  
 Bensby, T., Feltzing, S., & Oey, M. S. 2014, *A&A*, 562, A71  
 Bergemann, M., Pickering, J. C., & Gehren, T. 2010, *MNRAS*, 401, 1334  
 Blanco-Cuaresma, S. 2019, *MNRAS*, 486, 2075  
 Blanco-Cuaresma, S., Soubiran, C., Heiter, U., & Jofré, P. 2014, *A&A*, 569, A111  
 Bodaghe, A., Santos, N. C., Israelian, G., & Mayor, M. 2003, *A&A*, 404, 715  
 Booth, A. J. & Blackwell, D. E. 1983, *MNRAS*, 204, 777  
 Borsa, F., Allart, R., Casasayas-Barris, N., et al. 2021, *A&A*, 645, A24  
 Bravo, E. & Martínez-Pinedo, G. 2012, *Phys. Rev. C*, 85, 055805  
 Bressan, A., Marigo, P., Girardi, L., et al. 2012, *MNRAS*, 427, 127  
 Brewer, M.-M. & Carney, B. W. 2006, *AJ*, 131, 431  
 Buchhave, L. A., Bizzarro, M., Latham, D. W., et al. 2014, *Nature*, 509, 593  
 Caballero, J. A., Cortés-Contreras, M., Alonso-Floriano, F. J., et al. 2016a, in 19th Cambridge Workshop on Cool Stars, Stellar Systems, and the Sun (CS19), Cambridge Workshop on Cool Stars, Stellar Systems, and the Sun, 148  
 Caballero, J. A., Guàrdia, J., López del Fresno, M., et al. 2016b, in Society of Photo-Optical Instrumentation Engineers (SPIE) Conference Series, Vol. 9910, Observatory Operations: Strategies, Processes, and Systems VI, ed. A. B. Peck, R. L. Seaman, & C. R. Benn, 99100E  
 Chen, Y., Girardi, L., Bressan, A., et al. 2014, *MNRAS*, 444, 2525  
 Clayton, D. 2003, *Handbook of Isotopes in the Cosmos*  
 Condon, E. U. & Shortley, G. H. 1963, *The theory of atomic spectra*  
 Cortés-Contreras, M. 2017, PhD thesis, Universidad Complutense de Madrid, Spain  
 del Peloso, E. F., Cunha, K., da Silva, L., & Porto de Mello, G. F. 2005, *A&A*, 441, 1149  
 Den Hartog, E. A., Lawler, J. E., & Wood, M. P. 2014, *ApJS*, 215, 7  
 Dorn, C., Khan, A., Heng, K., et al. 2015, *A&A*, 577, A83

- Ernandes, H., Barbuy, B., Alves-Brito, A., et al. 2018, *A&A*, 616, A18
- Fabbian, D., Nissen, P. E., Asplund, M., Pettini, M., & Akerman, C. 2009, *A&A*, 500, 1143
- Feltzing, S. & Gustafsson, B. 1998, *A&AS*, 129, 237
- Fischer, D. A. & Valenti, J. 2005, *ApJ*, 622, 1102
- Gilli, G., Israelian, G., Ecuivillon, A., Santos, N. C., & Mayor, M. 2006, *A&A*, 449, 723
- Gratton, R. G. & Sneden, C. 1991, *A&A*, 241, 501
- Gray, D. F. 1992, *The observation and analysis of stellar photospheres.*, Vol. 20 (Cambridge University Press)
- Gray, D. F. & Brown, K. I. T. 2006, *PASP*, 118, 1112
- Gustafsson, B., Edvardsson, B., Eriksson, K., et al. 2008, *A&A*, 486, 951
- Hawkins, K., Masseron, T., Jofré, P., et al. 2016, *A&A*, 594, A43
- Hinkel, N. R., Timmes, F. X., Young, P. A., Pagano, M. D., & Turnbull, M. C. 2014, *AJ*, 148, 54
- Hinkel, N. R., Young, P. A., Pagano, M. D., et al. 2016, *ApJS*, 226, 4
- Hinkle, K., Wallace, L., Valenti, J., & Harmer, D. 2000, *Visible and Near Infrared Atlas of the Arcturus Spectrum 3727-9300 Å*
- Husser, T. O., Wende-von Berg, S., Dreizler, S., et al. 2013, *A&A*, 553, A6
- Ishikawa, H. T., Aoki, W., Kotani, T., et al. 2020, *PASJ*, 72, 102
- Jofré, E., Petrucci, R., Saffe, C., et al. 2015a, *A&A*, 574, A50
- Jofré, P., Heiter, U., & Soubiran, C. 2019, *ARA&A*, 57, 571
- Jofré, P., Heiter, U., Soubiran, C., et al. 2015b, *A&A*, 582, A81
- Jofré, P., Heiter, U., Worley, C. C., et al. 2017, *A&A*, 601, A38
- Johnson, J. A., Aller, K. M., Howard, A. W., & Crepp, J. R. 2010, *PASP*, 122, 905
- Kobayashi, C., Karakas, A. I., & Lugaro, M. 2020, *ApJ*, 900, 179
- Kobayashi, C., Karakas, A. I., & Umeda, H. 2011, *MNRAS*, 414, 3231
- Kobayashi, C., Umeda, H., Nomoto, K., Tominaga, N., & Ohkubo, T. 2006, *ApJ*, 653, 1145
- Kurucz, R. L. 2011, *Canadian Journal of Physics*, 89, 417
- Lawler, J. E., Wood, M. P., Den Hartog, E. A., et al. 2014, *ApJS*, 215, 20
- Lindgren, S., Heiter, U., & Seifahrt, A. 2016, *A&A*, 586, A100
- Liu, F., Chen, Y. Q., Zhao, G., et al. 2012, *MNRAS*, 422, 2969
- Liu, Y. J., Zhao, G., Shi, J. R., Pietrzyński, G., & Gieren, W. 2007, *MNRAS*, 382, 553
- Lomaeva, M., Jönsson, H., Ryde, N., Schultheis, M., & Thorsbro, B. 2019, *A&A*, 625, A141
- Maldonado, J., Eiroa, C., Villaver, E., Montesinos, B., & Mora, A. 2015, *A&A*, 579, A20
- Maldonado, J., Micela, G., Baratella, M., et al. 2020, *A&A*, 644, A68
- Mann, A. W., Brewer, J. M., Gaidos, E., Lépine, S., & Hilton, E. J. 2013, *AJ*, 145, 52
- Marfil, E., Tabernero, H. M., Montes, D., et al. 2021, *A&A*, submitted
- McWilliam, A., Wallerstein, G., & Mottini, M. 2013, *ApJ*, 778, 149
- Meléndez, J., Asplund, M., Gustafsson, B., & Yong, D. 2009, *ApJ*, 704, L66
- Montes, D., González-Peinado, R., Tabernero, H. M., et al. 2018, *MNRAS*, 479, 1332
- Montes, D., López-Santiago, J., Gálvez, M. C., et al. 2001, *MNRAS*, 328, 45
- Nagel, E. 2019, PhD thesis, Universität Hamburg
- Neves, V., Santos, N. C., Sousa, S. G., Correia, A. C. M., & Israelian, G. 2009, *A&A*, 497, 563
- Newton, E. R., Charbonneau, D., Irwin, J., et al. 2014, *AJ*, 147, 20
- Nomoto, K., Kobayashi, C., & Tominaga, N. 2013, *ARA&A*, 51, 457
- North, P., Cescutti, G., Jablonka, P., et al. 2012, *A&A*, 541, A45
- Olander, T., Heiter, U., & Kochukhov, O. 2021, *A&A*, 649, A103
- Ou, X., Roederer, I. U., Sneden, C., et al. 2020, *ApJ*, 900, 106
- Pakhomov, Y., Piskunov, N., & Ryabchikova, T. 2017, in *Astronomical Society of the Pacific Conference Series*, Vol. 510, *Stars: From Collapse to Collapse*, ed. Y. Y. Balega, D. O. Kudryavtsev, I. I. Romanyuk, & I. A. Yakunin, 518
- Pakhomov, Y. V., Ryabchikova, T. A., & Piskunov, N. E. 2019, *Astronomy Reports*, 63, 1010
- Palle, E., Luque, R., Zapatero Osorio, M. R., et al. 2021, *A&A*, 650, A55
- Passegger, V. M., Reiners, A., Jeffers, S. V., et al. 2018, *A&A*, 615, A6
- Passegger, V. M., Schweitzer, A., Shulyak, D., et al. 2019, *A&A*, 627, A161
- Peterson, R. C., Kurucz, R. L., & Ayres, T. R. 2017, *ApJS*, 229, 23
- Petigura, E. A., Marcy, G. W., Winn, J. N., et al. 2018, *AJ*, 155, 89
- Plez, B. 2012, *Turbospectrum: Code for spectral synthesis*
- Prochaska, J. X. & McWilliam, A. 2000, *ApJ*, 537, L57
- Prochaska, J. X., Naumov, S. O., Carney, B. W., McWilliam, A., & Wolfe, A. M. 2000, *AJ*, 120, 2513
- Quirrenbach, A., Amado, P. J., Caballero, J. A., et al. 2014, in *Society of Photo-Optical Instrumentation Engineers (SPIE) Conference Series*, Vol. 9147, *Ground-based and Airborne Instrumentation for Astronomy V*, ed. S. K. Ramsay, I. S. McLean, & H. Takami, 91471F
- Quirrenbach, A., Amado, P. J., Ribas, I., et al. 2018, in *Society of Photo-Optical Instrumentation Engineers (SPIE) Conference Series*, Vol. 10702, *Ground-based and Airborne Instrumentation for Astronomy VII*, ed. C. J. Evans, L. Simard, & H. Takami, 107020W
- Quirrenbach, A., CARMENES Consortium, Amado, P. J., et al. 2020, in *Society of Photo-Optical Instrumentation Engineers (SPIE) Conference Series*, Vol. 11447, *Society of Photo-Optical Instrumentation Engineers (SPIE) Conference Series*, 114473C
- Ramírez, I., Meléndez, J., Bean, J., et al. 2014, *A&A*, 572, A48
- Reddy, B. E., Lambert, D. L., & Allende Prieto, C. 2006, *MNRAS*, 367, 1329
- Reddy, B. E., Tomkin, J., Lambert, D. L., & Allende Prieto, C. 2003, *MNRAS*, 340, 304
- Reiners, A., Zechmeister, M., Caballero, J. A., et al. 2018, *A&A*, 612, A49
- Roederer, I. U., Preston, G. W., Thompson, I. B., et al. 2014, *AJ*, 147, 136
- Rojas-Ayala, B., Covey, K. R., Muirhead, P. S., & Lloyd, J. P. 2012, *ApJ*, 748, 93
- Sarmiento, P., Rojas-Ayala, B., Delgado Mena, E., & Blanco-Cuaresma, S. 2021, *A&A*, 649, A147
- Schweitzer, A., Passegger, V. M., Cifuentes, C., et al. 2019, *A&A*, 625, A68
- Scott, P., Asplund, M., Grevesse, N., Bergemann, M., & Sauval, A. J. 2015, *A&A*, 573, A26
- Smette, A., Sana, H., Noll, S., et al. 2015, *A&A*, 576, A77
- Snedden, C., Cowan, J. J., Kobayashi, C., et al. 2016, *ApJ*, 817, 53
- Snellen, I. A. G. 2004, *MNRAS*, 353, L1
- Sobelman, I. I. 2006, *Theory of Atomic Spectra*
- Souto, D., Cunha, K., García-Hernández, D. A., et al. 2017, *ApJ*, 835, 239
- Souto, D., Cunha, K., Smith, V. V., et al. 2020, *ApJ*, 890, 133
- Souto, D., Unterborn, C. T., Smith, V. V., et al. 2018, *ApJ*, 860, L15
- Tabernero, H. M., Dorda, R., Negueruela, I., & González-Fernández, C. 2018, *MNRAS*, 476, 3106
- Tabernero, H. M., Dorda, R., Negueruela, I., & Marfil, E. 2021, *A&A*, 646, A98
- Tabernero, H. M., Montes, D., & González Hernández, J. I. 2012, *A&A*, 547, A13
- Takeda, Y. 2007, *PASJ*, 59, 335
- Timmes, F. X., Woosley, S. E., & Weaver, T. A. 1995, *ApJS*, 98, 617
- Tinsley, B. M. 1980, *Fund. Cosmic Phys.*, 5, 287
- Veyette, M. J., Muirhead, P. S., Mann, A. W., et al. 2017, *ApJ*, 851, 26
- Vitas, N. & Vince, I. 2003, *Serbian Astronomical Journal*, 167, 35
- Wood, M. P., Lawler, J. E., Den Hartog, E. A., Sneden, C., & Cowan, J. J. 2014, *ApJS*, 214, 18
- Wood, M. P., Sneden, C., Lawler, J. E., et al. 2018, *ApJS*, 234, 25
- Woodgate, G. K. 1980, *Elementary Atomic Structure* (Oxford: Oxford Univ. Press)
- Woosley, S. E. & Weaver, T. A. 1995, *ApJS*, 101, 181
- Yan, F., Pallé, E., Reiners, A., et al. 2020, *A&A*, 640, L5
- Zechmeister, M., Anglada-Escudé, G., & Reiners, A. 2014, *A&A*, 561, A59
- Zechmeister, M., Reiners, A., Amado, P. J., et al. 2018, *A&A*, 609, A12

<sup>1</sup> Institut für Astrophysik, Georg-August-Universität, Friedrich-Hund-Platz 1, 37077 Göttingen, Germany  
e-mail: yutong.shan@uni-goettingen.de

<sup>2</sup> University of Applied Sciences Technikum Wien, Höchstädtplatz 6, 1200 Wien, Austria

<sup>3</sup> Fakultät für Mathematik, Universität Wien, Oskar-Morgenstern-Platz 1, 1090 Wien, Austria

<sup>4</sup> Departamento de Física de la Tierra y Astrofísica and IPARCOS-UCM (Instituto de Física de Partículas y del Cosmos de la UCM), Facultad de Ciencias Físicas, Universidad Complutense de Madrid, 28040, Madrid, Spain

<sup>5</sup> Centro de Astrobiología (CSIC-INTA), ESAC, Camino bajo del castillo s/n, 28692 Villanueva de la Cañada, Madrid, Spain

<sup>6</sup> Institut de Ciències de l'Espai (ICE, CSIC), Campus UAB, Can Magrans s/n, 08193 Bellaterra, Spain

<sup>7</sup> Institut d'Estudis Espacials de Catalunya (IEEC), 08034 Barcelona, Spain

<sup>8</sup> Landessternwarte, Zentrum für Astronomie der Universität Heidelberg, Königstuhl 12, 69117 Heidelberg, Germany

<sup>9</sup> Instituto de Astrofísica de Andalucía (CSIC), Glorieta de la Astronomía s/n, 18008 Granada, Spain

<sup>10</sup> Centro Astronómico Hispano-Alemán, Observatorio de Calar Alto, Sierra de los Filabres, 04550 Gérgal, Spain

<sup>11</sup> Instituto de Astrofísica de Canarias, 38205 La Laguna, Tenerife, Spain

<sup>12</sup> Departamento de Astrofísica, Universidad de La Laguna, 38206 La Laguna, Tenerife, Spain

<sup>13</sup> Thüringer Landessternwarte Tautenburg, Sternwarte 5, 07778 Tautenburg, Germany



- <sup>14</sup> Max-Planck-Institut für Astronomie, Königstuhl 17, 69117 Heidelberg, Germany
- <sup>15</sup> Max-Planck-Institut für Sonnensystemforschung, Justus-von-Liebig-Weg 3, 37077 Göttingen, Germany
- <sup>16</sup> Department of Physics, University of Warwick, Gibbet Hill Road, Coventry CV4 7AL, United Kingdom
- <sup>17</sup> Hamburger Sternwarte, Universität Hamburg, Gojenbergsweg 112, 21029 Hamburg, Germany
- <sup>18</sup> Homer L. Dodge Department of Physics and Astronomy, University of Oklahoma, 440 West Brooks Street, Norman, OK 73019, United States of America

## **Appendix A: Long Table**

Table A.1 is available in its entirety in electronic form at the CDS via anonymous ftp to [cdsarc.u-strasbg.fr](ftp://cdsarc.u-strasbg.fr) (130.79.128.5) or via <http://cdsweb.u-strasbg.fr/cgi-bin/qcat?J/A+A/>.

**Table A.1.** Measured vanadium abundances for the sample

Karmn	SpT	$v \sin i^a$ (km/s)	Schw19 Stellar Parameters					Marfil+ Stellar Parameters					Kinematic Membership
			$T_{\text{eff}}$ (K)	$\log g$	[Fe/H]	[V/H]	$\delta[\text{V}/\text{H}]^b$	$T_{\text{eff}}$ (K)	$\log g$	[Fe/H]	[V/H]	$\delta[\text{V}/\text{H}]^b$	
J00051+457	M1.0V	2.0	3675	4.84	-0.16	-0.01	0.03	3759	4.72	-0.02	0.02	0.04	YD
J00183+440	M1.0V	2.0	3615	4.91	-0.25	-0.25	0.07	3613	4.86	-0.47	-0.31	0.06	D
J00389+306	M2.5V	2.0	3537	4.89	-0.05	-0.04	0.06	3559	4.81	-0.18	-0.10	0.06	D
J01013+613	M2.0V	2.0	3529	4.94	-0.16	-0.15	0.06	3562	4.81	-0.24	-0.20	0.06	D
J01025+716	M3.0V	2.0	3488	4.91	0.02	0.06	0.07	3523	4.76	-0.06	0.00	0.07	D
J01026+623	M1.5V	2.0	3805	4.69	0.13	0.13	0.04	3806	4.71	0.02	0.12	0.04	YD
J01433+043	M2.0V	2.0	3532	4.91	-0.09	-0.09	0.06	3550	4.82	-0.20	-0.14	0.06	D
J01518+644	M2.5V	2.0	3555	4.90	-0.08	0.06	0.03	3648	4.55	-0.02	-0.05	0.04	YD
J02015+637	M3.0V	2.0	3489	4.93	-0.05	0.09	0.05	3563	4.81	-0.13	0.05	0.04	D
J02123+035	M1.5V	2.0	3663	4.81	-0.05	-0.24	0.07	3595	4.87	-0.49	-0.35	0.04	TD
J02222+478	M0.5V	2.0	3935	4.67	0.07	0.10	0.03	3899	4.67	0.00	0.09	0.03	D
J02358+202	M2.0V	2.0	3585	4.89	-0.13	0.08	0.04	3715	4.55	0.00	0.02	0.05	YD
J02442+255	M3.0V	2.0	3472	4.95	-0.06	-0.06	0.07	3495	4.88	-0.14	-0.09	0.07	YD
J02565+554W	M1.0V	2.0	3896	4.66	0.18	0.16	0.03	3828	4.68	-0.03	0.14	0.02	D
J03181+382	M1.5V	2.0	3861	4.66	0.20	0.27	0.03	3845	4.68	0.10	0.25	0.03	D
J03213+799	M2.0V	2.0	3549	4.93	-0.18	-0.14	0.06	3592	4.80	-0.23	-0.18	0.06	D
J03217-066	M2.0V	2.0	3555	4.92	-0.15	0.00	0.06	3653	4.75	-0.04	-0.01	0.05	YD
J03463+262	M0.0V	3.3	3993	4.65	0.12	0.13	0.03	3965	4.69	-0.01	0.14	0.02	YD
J03531+625	M3.0V	2.0	3488	4.93	-0.04	-0.13	0.07	3496	4.84	-0.18	-0.20	0.07	TD
J04225+105	M3.5V	2.0	3445	4.95	0.00	0.16	0.05	3526	4.79	-0.04	0.13	0.05	YD
J04290+219	M0.5V	3.9	4199	4.59	0.23	0.31	0.02	4143	4.63	0.12	0.30	0.02	D
J04376+528	M0.0V	3.4	4034	4.68	-0.09	-0.07	0.03	4031	4.66	-0.06	-0.07	0.03	D
J04376-110	M1.5V	2.0	3621	4.85	-0.07	-0.02	0.04	3651	4.81	-0.11	-0.04	0.04	D
J04429+189	M2.0V	2.0	3574	4.89	-0.10	0.07	0.04	3674	4.71	0.00	0.04	0.04	D
J04429+214	M3.5V	2.0	3437	4.97	-0.03	0.05	0.06	3511	4.77	-0.01	0.02	0.06	D
J04538-177	M2.0V	2.0	3572	4.90	-0.12	-0.14	0.06	3573	4.88	-0.31	-0.20	0.06	D
J04588+498	M0.0V	2.0	4022	4.65	0.09	0.10	0.03	3994	4.67	0.02	0.09	0.03	D
J05127+196	M2.0V	2.0	3582	4.90	-0.13	-0.07	0.05	3614	4.79	-0.26	-0.14	0.04	D
J05314-036	M1.5V	2.0	3891	4.64	0.23	0.29	0.04	3871	4.65	0.13	0.29	0.03	D
J05365+113	M0.0V	3.8	4074	4.65	0.05	0.03	0.03	4064	4.68	0.00	0.02	0.02	YD
J05415+534	M1.0V	2.0	3875	4.69	0.08	0.09	0.04	3859	4.54	0.03	0.00	0.04	YD
J06103+821	M2.0V	2.0	3521	4.92	-0.11	-0.06	0.06	3546	4.82	-0.17	-0.10	0.06	D
J06105-218	M0.5V	2.0	3837	4.70	0.07	0.09	0.04	3829	4.71	0.00	0.09	0.04	YD
J06421+035	M3.5V	2.0	3454	4.95	0.00	0.00	0.06	3498	4.77	-0.08	-0.06	0.06	D
J06548+332	M3.0V	2.0	3451	4.96	-0.03	-0.01	0.07	3528	4.86	-0.17	-0.05	0.06	YD
J07044+682	M3.0V	2.0	3461	4.95	-0.04	0.04	0.06	3543	4.82	-0.10	0.01	0.06	D
J07287-032	M3.0V	2.0	3466	4.94	-0.03	0.00	0.06	3504	4.84	-0.18	-0.06	0.06	D
J07353+548	M2.0V	2.0	3520	4.94	-0.16	-0.15	0.06	3567	4.84	-0.25	-0.18	0.06	YD
J07361-031	M1.0V	3.1	3894	4.69	0.05	-0.04	0.05	3834	4.70	0.00	-0.05	0.04	D
J07393+021	M0.0V	2.0	4014	4.66	0.07	0.10	0.03	3991	4.53	-0.01	0.02	0.03	YD
J08161+013	M2.0V	2.0	3568	4.89	-0.10	-0.06	0.05	3586	4.80	-0.25	-0.12	0.05	D
J08293+039	M2.5V	2.0	3585	4.88	-0.08	0.07	0.04	3675	4.55	-0.01	-0.03	0.04	YD
J08358+680	M2.5V	2.0	3461	4.98	-0.11	-0.10	0.07	3498	4.77	-0.06	-0.13	0.08	D

**Table A.1.** Measured vanadium abundances for the sample

Karmn	SpT	$v \sin i^a$ (km/s)	Schw19 Stellar Parameters					Marfil+ Stellar Parameters					Kinematic Membership
			$T_{\text{eff}}$ (K)	$\log g$	[Fe/H]	[V/H]	$\delta[\text{V}/\text{H}]^b$	$T_{\text{eff}}$ (K)	$\log g$	[Fe/H]	[V/H]	$\delta[\text{V}/\text{H}]^b$	
J09133+688	M2.5V	2.0	3555	4.92	-0.16	0.02	0.04	3699	4.73	0.09	0.05	0.05	YD
J09140+196	M3.0V	2.0	3493	4.95	-0.10	0.08	0.05	3565	4.56	-0.04	-0.04	0.05	YD
J09143+526	M0.0V	2.0	4024	4.68	-0.05	-0.05	0.03	3992	4.71	-0.14	-0.04	0.02	YD
J09144+526	M0.0V	2.3	4005	4.68	-0.03	-0.03	0.03	3992	4.69	-0.06	-0.03	0.03	YD
J09163-186	M1.5V	2.0	3585	4.91	-0.18	-0.05	0.06	3707	4.73	-0.01	-0.02	0.06	YD
J09360-216	M2.5V	2.0	3505	4.94	-0.12	-0.16	0.09	3494	4.84	-0.27	-0.24	0.08	D
J09411+132	M1.5V	2.0	3613	4.87	-0.11	-0.02	0.05	3695	4.73	-0.07	-0.05	0.04	YD
J09425+700	M2.0V	2.0	3515	4.94	-0.12	0.10	0.05	3574	4.77	-0.07	0.08	0.04	YD
J09468+760	M1.5V	2.0	3680	4.78	-0.01	-0.10	0.05	3628	4.78	-0.27	-0.18	0.05	TD
J09511-123	M0.5V	2.0	3777	4.76	-0.07	-0.10	0.04	3737	4.74	-0.29	-0.16	0.04	TD
J09561+627	M0.0V	2.0	3980	4.66	0.07	0.09	0.03	3957	4.69	0.00	0.11	0.02	YD
J10023+480	M1.0V	2.0	3785	4.72	0.05	0.01	0.03	3758	4.73	-0.17	-0.04	0.02	TD
J10122-037	M1.5V	2.0	3610	4.87	-0.13	0.07	0.04	3722	4.73	-0.04	0.08	0.04	YD
J10167-119	M3.0V	2.0	3532	4.88	0.01	0.08	0.05	3561	4.81	-0.10	0.04	0.05	D
J10251-102	M1.0V	2.0	3780	4.72	0.06	0.08	0.05	3746	4.72	-0.06	0.05	0.04	YD
J10289+008	M2.0V	2.0	3579	4.88	-0.09	-0.10	0.05	3586	4.59	-0.18	-0.24	0.06	YD
J10350-094	M3.0V	2.0	3469	4.94	-0.02	0.03	0.06	3546	4.82	-0.16	-0.02	0.05	D
J10396-069	M2.5V	2.0	3554	4.88	-0.02	0.11	0.05	3596	4.76	-0.08	0.05	0.04	YD
J11000+228	M2.5V	2.0	3499	4.94	-0.11	-0.08	0.06	3518	4.60	-0.11	-0.21	0.07	YD
J11026+219	M1.0V	2.6	3905	4.69	0.04	-0.01	0.04	3872	4.70	0.00	-0.02	0.04	D
J11054+435	M1.0V	2.0	3639	4.92	-0.30	-0.34	0.07	3639	4.92	-0.53	-0.38	0.06	TD-D
J11110+304	M2.0V	2.0	3753	4.71	0.13	0.18	0.04	3739	4.69	-0.04	0.13	0.04	D
J11126+189	M1.5V	2.0	3645	4.86	-0.14	0.05	0.03	3735	4.70	-0.08	0.05	0.04	D
J11302+076	M2.5V	2.0	3513	4.91	-0.03	0.07	0.05	3563	4.59	-0.10	-0.07	0.05	D
J11306-080	M3.5V	2.0	3422	4.98	-0.01	0.02	0.07	3491	4.78	-0.04	-0.02	0.07	YD
J11467-140	M3.0V	2.0	3570	4.82	0.11	0.24	0.05	3629	4.72	0.00	0.17	0.04	D
J11511+352	M1.5V	2.0	3645	4.87	-0.17	-0.14	0.05	3704	4.70	-0.06	-0.14	0.06	D
J12123+544S	M0.0V	2.0	3933	4.70	-0.03	-0.04	0.03	3910	4.73	-0.10	-0.05	0.03	D
J12230+640	M3.0V	2.0	3540	4.86	0.05	0.08	0.06	3578	4.80	-0.15	0.01	0.05	D
J12248-182	M2.0V	2.0	3485	4.98	-0.17	-0.34	0.11	3476	4.93	-0.48	-0.45	0.08	TD
J12312+086	M0.5V	2.0	3914	4.71	-0.07	-0.04	0.03	3919	4.67	-0.06	-0.05	0.03	D
J12350+098	M2.5V	2.0	3572	4.85	0.02	-0.03	0.07	3563	4.81	-0.21	-0.11	0.07	D
J12388+116	M3.0V	2.0	3439	4.96	0.00	0.14	0.05	3511	4.77	0.00	0.11	0.05	D
J13196+333	M1.5V	2.0	3812	4.67	0.18	0.24	0.04	3792	4.54	-0.02	0.15	0.03	YD
J13209+342	M1.0V	2.0	3763	4.73	0.03	-0.01	0.04	3760	4.73	-0.21	-0.06	0.04	D
J13283-023W	M3.0V	2.0	3482	4.92	0.01	0.11	0.07	3554	4.75	-0.07	0.07	0.06	D
J13299+102	M0.5V	2.0	3714	4.81	-0.15	-0.06	0.05	3779	4.73	-0.11	-0.06	0.05	D
J13450+176	M0.0V	2.3	3806	4.85	-0.43	-0.44	0.05	3816	4.83	-0.60	-0.46	0.04	TD
J13457+148	M1.5V	2.0	3678	4.79	-0.04	-0.15	0.06	3619	4.86	-0.40	-0.23	0.04	D
J14010-026	M1.0V	2.0	3724	4.77	-0.04	-0.05	0.04	3710	4.75	-0.22	-0.10	0.04	D
J14082+805	M1.0V	2.0	3841	4.67	0.16	0.11	0.04	3803	4.68	-0.03	0.09	0.03	D
J14251+518	M2.5V	2.0	3521	4.91	-0.07	-0.03	0.06	3558	4.81	-0.20	-0.09	0.06	D
J14257+236E	M0.5V	2.0	3947	4.65	0.17	0.20	0.03	3907	4.67	0.01	0.19	0.02	TD-D

**Table A.1.** Measured vanadium abundances for the sample

Karmn	SpT	$v \sin i^a$ (km/s)	Schw19 Stellar Parameters					Marfil+ Stellar Parameters					Kinematic Membership
			$T_{\text{eff}}$ (K)	$\log g$	[Fe/H]	[V/H]	$\delta[\text{V}/\text{H}]^b$	$T_{\text{eff}}$ (K)	$\log g$	[Fe/H]	[V/H]	$\delta[\text{V}/\text{H}]^b$	
J14257+236W	M0.0V	2.0	4024	4.64	0.17	0.22	0.03	3983	4.67	0.07	0.22	0.02	D
J14294+155	M2.0V	2.0	3671	4.76	0.06	0.07	0.04	3653	4.72	-0.08	0.01	0.04	TD
J14307-086	M0.5V	2.4	4089	4.63	0.14	0.18	0.02	4026	4.66	0.02	0.17	0.01	TD-D
J14524+123	M2.0V	2.0	3548	4.89	-0.08	0.19	0.04	3714	4.70	0.07	0.21	0.05	D
J15095+031	M3.0V	2.0	3492	4.92	-0.01	0.05	0.06	3545	4.82	-0.10	0.01	0.05	D
J15194-077	M3.0V	2.0	3441	4.98	-0.08	-0.10	0.09	3488	4.88	-0.18	-0.13	0.07	YD
J15598-082	M1.0V	2.0	3625	4.89	-0.19	-0.06	0.04	3728	4.70	-0.01	-0.03	0.05	D
J16167+672N	M3.0V	2.0	3488	4.93	-0.03	0.10	0.08	3575	4.74	-0.04	0.06	0.07	YD
J16167+672S	M0.0V	2.7	4090	4.62	0.15	0.19	0.04	4054	4.66	0.07	0.20	0.03	D
J16254+543	M1.5V	2.0	3525	4.97	-0.26	-0.30	0.08	3588	4.90	-0.34	-0.31	0.06	YD
J16462+164	M2.5V	2.0	3506	4.92	-0.06	0.03	0.05	3558	4.81	-0.11	0.00	0.05	D
J16581+257	M1.0V	2.0	3734	4.78	-0.08	0.01	0.04	3780	4.73	-0.11	0.00	0.04	D
J17052-050	M1.5V	2.0	3642	4.81	-0.01	-0.14	0.07	3597	4.87	-0.37	-0.21	0.06	TD-D
J17166+080	M2.0V	2.0	3543	4.91	-0.10	-0.07	0.06	3567	4.81	-0.23	-0.13	0.06	YD
J17303+055	M0.0V	2.0	3812	4.77	-0.15	-0.06	0.03	3825	4.57	-0.19	-0.15	0.03	YD
J17355+616	M0.5V	2.0	3893	4.69	0.06	0.07	0.05	3878	4.67	0.00	0.04	0.05	D
J17378+185	M1.0V	2.0	3656	4.87	-0.23	-0.22	0.05	3675	4.83	-0.37	-0.25	0.05	D
J18051-030	M1.0V	2.0	3663	4.86	-0.20	-0.16	0.06	3725	4.74	-0.19	-0.15	0.06	D
J18198-019	K7.0V	2.0	4143	4.66	-0.11	-0.06	0.02	4162	4.69	-0.12	-0.04	0.02	YD
J18353+457	M0.5V	2.0	3932	4.68	0.06	0.02	0.03	3896	4.67	-0.05	0.00	0.03	D
J18409-133	M1.0V	2.0	3812	4.70	0.08	0.11	0.04	3782	4.69	-0.05	0.09	0.03	D
J18480-145	M2.5V	2.0	3496	4.94	-0.11	-0.08	0.07	3540	4.82	-0.15	-0.12	0.07	D
J18580+059	M0.5V	2.0	3923	4.68	0.08	0.08	0.03	3898	4.67	-0.01	0.07	0.03	D
J19070+208	M2.0V	2.0	3536	4.94	-0.20	-0.29	0.11	3541	4.90	-0.49	-0.37	0.08	D
J19072+208	M2.0V	2.0	3526	4.96	-0.23	-0.30	0.10	3576	4.88	-0.43	-0.34	0.08	D
J19169+051N	M2.5V	2.0	3534	4.90	-0.04	0.09	0.05	3587	4.80	-0.14	0.03	0.04	D
J19346+045	M0.0V	3.9	4062	4.69	-0.17	-0.15	0.04	4047	4.68	-0.27	-0.17	0.03	D
J20450+444	M1.5V	2.0	3586	4.89	-0.15	-0.10	0.07	3615	4.82	-0.25	-0.15	0.06	YD
J20533+621	M1.0V	2.0	3843	4.71	0.04	0.03	0.04	3815	4.68	-0.07	0.01	0.03	D
J20567-104	M2.5V	2.0	3514	4.91	-0.03	0.09	0.05	3571	4.74	-0.08	0.03	0.05	TD
J21019-063	M2.5V	2.0	3507	4.92	-0.08	0.05	0.04	3560	4.75	-0.06	0.02	0.04	D
J21152+257	M3.0V	2.0	3675	4.68	0.29	0.28	0.05	3700	4.67	0.13	0.27	0.04	D
J21164+025	M3.0V	2.0	3485	4.94	-0.08	0.05	0.06	3552	4.60	-0.11	-0.07	0.06	YD
J21221+229	M1.0V	2.0	3705	4.83	-0.20	-0.11	0.05	3755	4.73	-0.21	-0.13	0.05	D
J21348+515	M3.0V	2.0	3497	4.91	0.00	0.00	0.06	3523	4.86	-0.13	-0.04	0.06	YD
J22021+014	M0.5V	2.0	3915	4.69	0.03	0.05	0.03	3904	4.67	-0.02	0.03	0.03	D
J22057+656	M1.5V	2.0	3653	4.86	-0.17	-0.08	0.04	3727	4.74	-0.11	-0.07	0.05	D
J22096-046	M3.5V	2.0	3467	4.94	-0.02	0.16	0.05	3579	4.77	-0.03	0.13	0.05	YD
J22115+184	M2.0V	2.0	3550	4.93	-0.13	0.18	0.03	3723	4.70	0.00	0.19	0.04	D
J22125+085	M3.0V	2.0	3501	4.92	-0.04	-0.05	0.07	3513	4.83	-0.16	-0.12	0.07	D
J22330+093	M1.0V	2.0	3669	4.86	-0.20	-0.15	0.04	3732	4.78	-0.26	-0.14	0.04	YD
J22503-070	M0.5V	2.0	3904	4.72	-0.10	-0.06	0.03	3911	4.70	-0.10	-0.07	0.03	D
J22559+178	M1.0V	2.0	3834	4.70	0.06	0.06	0.04	3808	4.68	-0.03	0.05	0.04	D

**Table A.1.** Measured vanadium abundances for the sample

Karmn	SpT	$v \sin i^a$ (km/s)	Schw19 Stellar Parameters					Marfil+ Stellar Parameters					Kinematic Membership
			$T_{\text{eff}}$ (K)	$\log g$	[Fe/H]	[V/H]	$\delta[\text{V}/\text{H}]^b$	$T_{\text{eff}}$ (K)	$\log g$	[Fe/H]	[V/H]	$\delta[\text{V}/\text{H}]^b$	
J22565+165	M1.5V	2.0	3805	4.69	0.12	0.15	0.04	3787	4.69	0.00	0.14	0.03	D
J23245+578	M1.0V	2.0	3842	4.68	0.14	0.18	0.03	3803	4.68	-0.02	0.15	0.02	D
J23340+001	M2.5V	2.0	3559	4.86	0.00	-0.09	0.06	3531	4.83	-0.20	-0.18	0.05	D
J23381-162	M2.0V	2.0	3551	4.91	-0.13	-0.16	0.08	3583	4.91	-0.35	-0.20	0.07	D
J23492+024	M1.0V	2.0	3653	4.84	-0.13	-0.35	0.09	3572	4.96	-0.61	-0.45	0.06	TD
J23556-061	M2.5V	2.0	3694	4.71	0.18	0.19	0.04	3698	4.70	0.03	0.16	0.03	D

**Notes.**

<sup>(a)</sup> a: the  $v \sin i$ 's given here are the rotational broadening parameters used for each star in the spectral fits. It is set to 2.0 km/s when the measurement (from Reiners et al. 2018) only gives an upper limit of 2.0 km/s, i.e., the true  $v \sin i \leq 2$  km/s.

<sup>(b)</sup> b: [V/H] error is given as the sample standard deviation of the fitted abundances over all line regions used for that particular star.

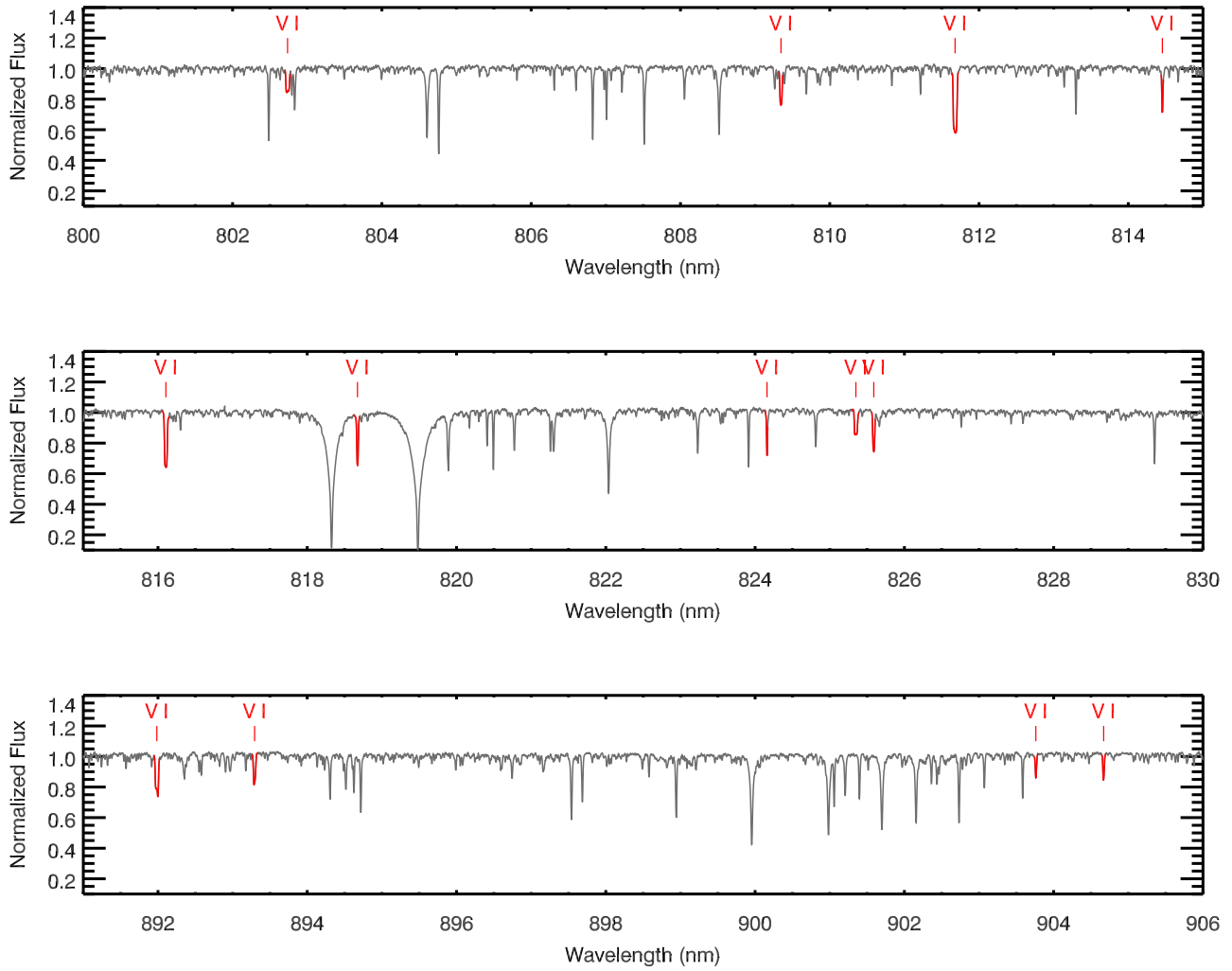


**Fig. B.1.** View of a representative, normalized, telluric-corrected and co-added CARMENES spectrum in the wavelength ranges considered in this work for a typical M0.0 V star (J14257+236W). The V I lines used in this study are marked in red.

**Appendix B: Representative CARMENES spectra in the wavelength region 800–910 nm**

**Appendix C: All fitted vanadium line regions**

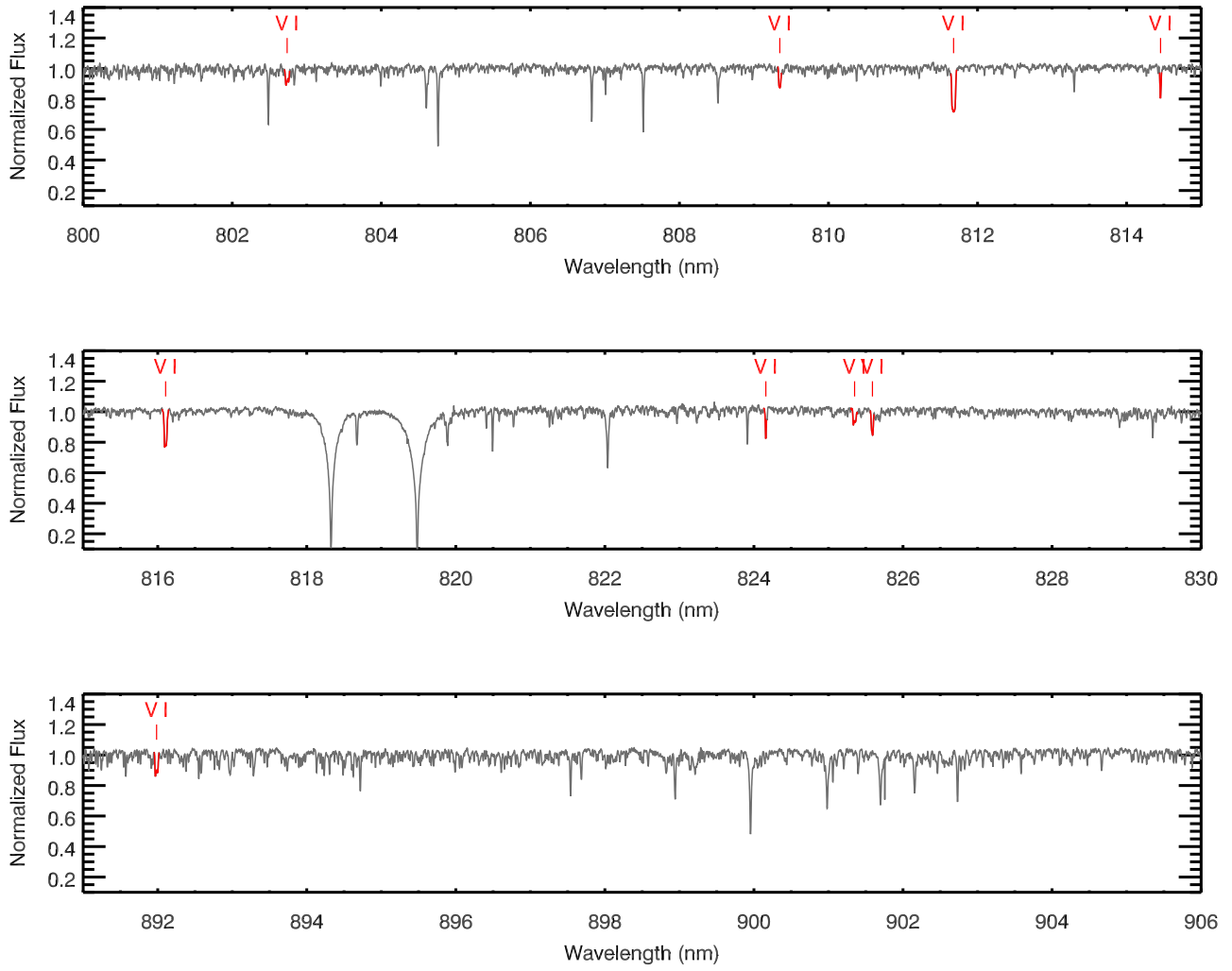


**Fig. B.2.** Same as Fig. B.1, but for a typical M2.0 V star (J03213+799).



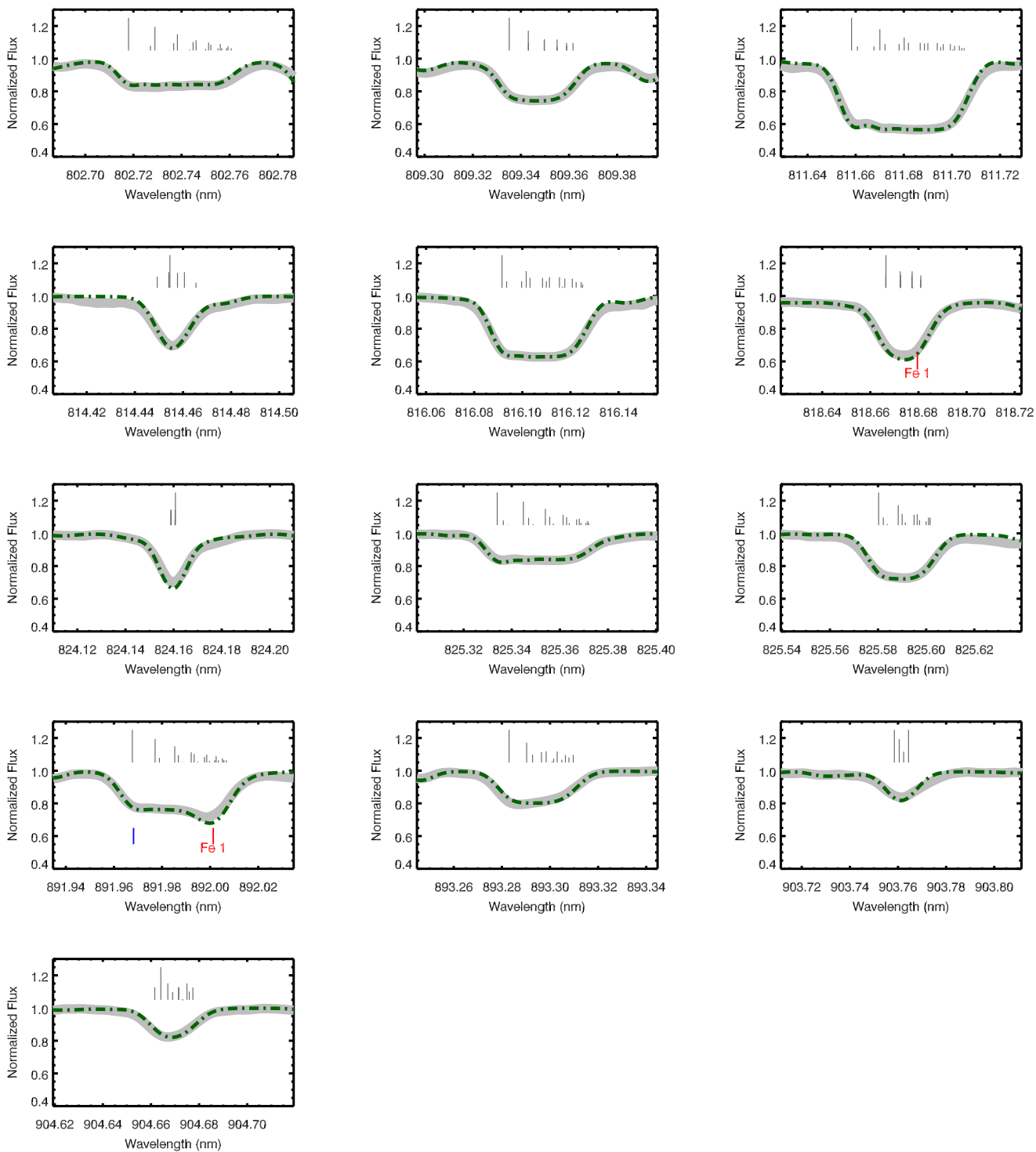


**Fig. C.1.** All V I line regions fitted to the observed CARMENES spectrum (thick gray) of a typical M0.0 V star (J14257+236W). The model corresponding to the best-fit V abundance, using the Schw19 stellar parameters, is shown in green dot-dashed lines. Individual V I HFS components and their relative strengths, as given by  $\log(gf\lambda) - \theta\chi$ , are shown in vertical gray lines above each feature. Notable contaminating lines (i.e., expected depth  $> 0.05$ ) inside the V I features from other species are marked in blue (for TiO) and red.

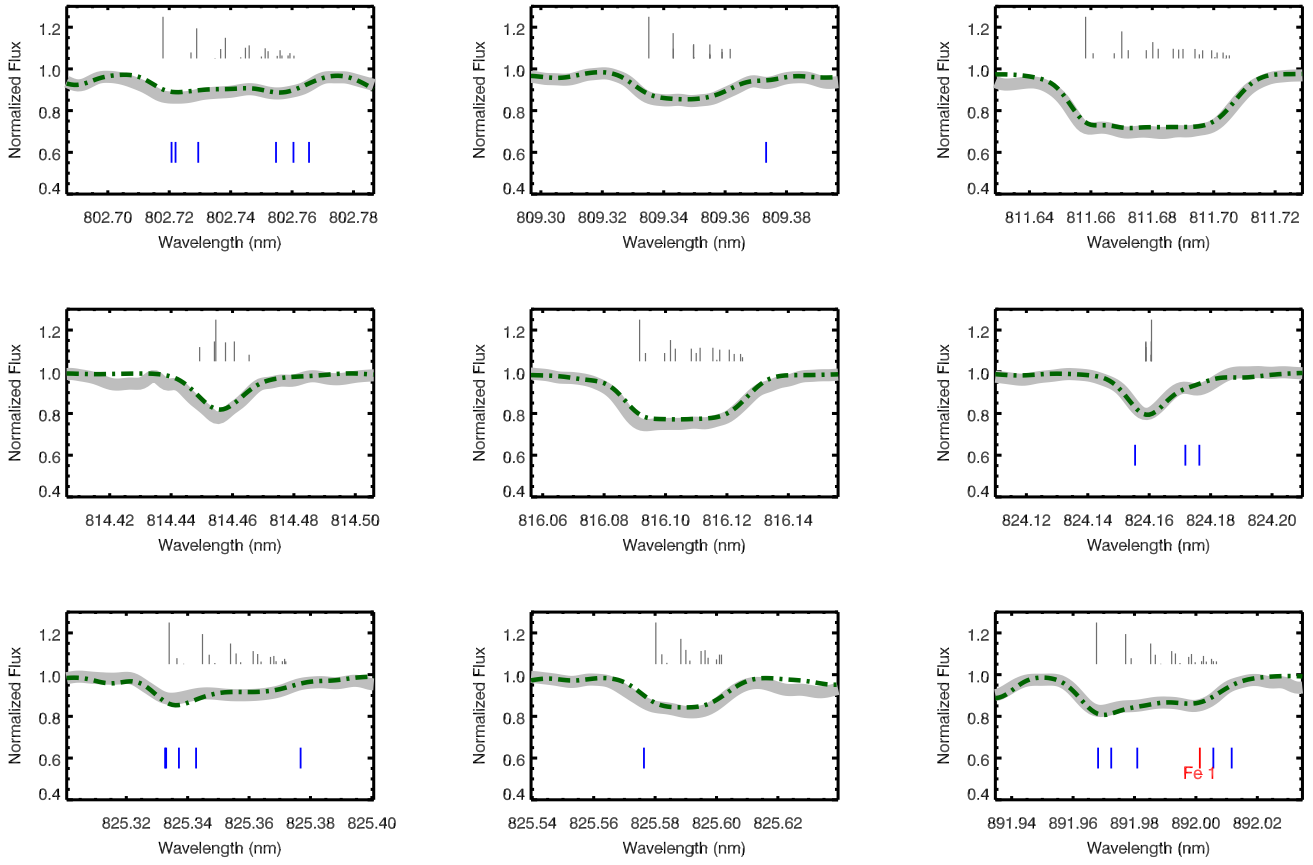


**Fig. C.2.** Same as Fig. C.1, but for a typical M2.0 V star (J03213+799).